PHYSICAL REVIEW D **96,** 034503 (2017)

Nucleon electromagnetic form factors using lattice simulations at the physical point

C. Alexandrou,[1,2] M. Constantinou,[3] K. Hadjiyiannakou,[1] K. Jansen,[4] Ch. Kallidonis,[1] G. Koutsou,[1] and A. Vaquero Aviles-Casco[5]

[1]*Computation-based Science and Technology Research Center, The Cyprus Institute, 20 Kavafi Street, Nicosia 2121, Cyprus*
[2]*Department of Physics, University of Cyprus, P.O. Box 20537, 1678 Nicosia, Cyprus*
[3]*Department of Physics, Temple University, 1925 North 12th Street, Philadelphia, Pennsylvania 19122-1801, USA*
[4]*NIC, DESY, Platanenallee 6, D-15738 Zeuthen, Germany*
[5]*Department of Physics and Astronomy, University of Utah, Salt Lake City, Utah 84112, USA*
(Received 2 June 2017; published 4 August 2017)

We present results for the nucleon electromagnetic form factors using an ensemble of maximally twisted mass clover-improved fermions with pion mass of about 130 MeV. We use multiple sink-source separations and three analysis methods to probe ground-state dominance. We evaluate both the connected and disconnected contributions to the nucleon matrix elements. We find that the disconnected quark loop contributions to the isoscalar matrix elements are small, giving an upper bound of up to 2% of the connected and smaller than its statistical error. We present results for the isovector and isoscalar electric and magnetic Sachs form factors and the corresponding proton and neutron form factors. By fitting the momentum dependence of the form factors to a dipole form or to the z expansion, we extract the nucleon electric and magnetic radii, as well as the magnetic moment. We compare our results to experiment as well as to other recent lattice QCD calculations.

DOI: 10.1103/PhysRevD.96.034503

I. INTRODUCTION

Electromagnetic form factors probe the internal structure of hadrons mapping their charge and magnetic distributions. The slope of the electric and magnetic form factors at zero momentum yields the electric and magnetic root mean square radius, while the value of the form factors at zero momentum gives its electric charge and magnetic moment. Extensive electron scattering experiments have been carried out since the fifties for the precise determination of the nucleon form factors, including recent experiments at Jefferson Lab, MIT-Bates and Mainz. For a recent review on electron elastic scattering experiments, see Ref. [1]. The proton radius can also be obtained spectroscopically, namely via the Lamb shifts of the hydrogen atom and of muonic hydrogen [2] and via transition frequencies of electronic and muonic deuterium. In these measurements, including a recent experiment using muonic deuterium [3], discrepancies are observed in the resulting proton radius between hydrogen and deuterium and their corresponding muonic equivalents. Whether new physics is responsible for this discrepancy, or errors in the theoretical or experimental analyses, a first principles calculation of the electromagnetic form factors of the nucleon can provide valuable insight. Although nucleon electromagnetic form factors have been extensively studied in lattice QCD, most of these studies have been carried out at higher than physical pion masses, requiring extrapolations to the physical point, which for the case of baryons carry a large systematic uncertainty.

In this paper, we calculate the electromagnetic form factors of the nucleon using an ensemble of two degenerate light quarks ($N_f = 2$) tuned to reproduce a pion mass of about 130 MeV, in a volume with $m_\pi L \simeq 3$ [4]. We use the twisted mass fermion action with clover improvement [5,6]. We employ $\mathcal{O}(10^5)$ measurements to reduce the statistical errors and multiple sink-source separations to study excited state effects using three different analyses. We extract the momentum dependence of the electric and magnetic Sachs form factors for both isovector and isoscalar combinations, i.e. for both the difference $(p - n)$ and sum $(p + n)$ of proton and neutron form factors. For the latter, we compute the computationally demanding disconnected contributions and find them to be smaller than the statistical errors of the connected contributions. To fit the momentum dependence we use both a dipole form as well as the z expansion [7]. From these fits, we extract the electric and magnetic radii, as well as the magnetic moments of the proton, the neutron and the isovector and isoscalar combinations. For the electric root mean squared (rms) radius of the proton we find $\sqrt{\langle r_E^2 \rangle_p} = 0.767(25)(21)$ fm where the first error is statistical and the second a systematic due to excited states. Although this value is closer to the value of 0.84087(39) fm extracted from muonic hydrogen [3], a more complete analysis of

systematic errors using multiple ensembles is required to assess accurately all lattice artifacts.

The remainder of this paper is organized as follows: in Sec. II, we provide details of the lattice setup for this calculation, and in Sec. III, we present our results. In Sec. IV, we compare our results with other lattice calculations and, in Sec. V, we summarize our findings and conclude.

II. SETUP AND LATTICE PARAMETERS

A. Electromagnetic form factors

The electromagnetic form factors are extracted from the electromagnetic nucleon matrix element given by

$$\langle N(p',s')|\mathcal{O}^V_\mu|N(p,s)\rangle = \sqrt{\frac{m_N^2}{E_N(\vec{p}')E_N(\vec{p})}}\bar{u}_N(p',s')\Lambda^V_\mu(q^2)u_N(p,s) \quad (1)$$

with $N(p,s)$ the nucleon state of momentum p and spin s, $E_N(\vec{p}) = p_0$ its energy and m_N its mass, $\vec{q} = \vec{p}' - \vec{p}$, the spatial momentum transfer from initial ($\vec{p}$) to final ($\vec{p}'$) momentum, u_N the nucleon spinor and $\mathcal{O}^V$ the vector current. In the isospin limit, where an exchange between up and down quarks ($u \leftrightarrow d$) and between proton and neutron ($p \leftrightarrow n$) is a symmetry, the isovector matrix element can be related to the difference between proton and neutron form factors as follows:

$$\langle p|\frac{2}{3}\bar{u}\gamma_\mu u - \frac{1}{3}\bar{d}\gamma_\mu d|p\rangle - \langle n|\frac{2}{3}\bar{u}\gamma_\mu u - \frac{1}{3}\bar{d}\gamma_\mu d|n\rangle \xrightarrow[p\leftrightarrow n]{u\leftrightarrow d} \langle p|\bar{u}\gamma_\mu u - \bar{d}\gamma_\mu d|p\rangle. \quad (2)$$

Similarly, for the isoscalar combination we have

$$\langle p|\frac{2}{3}\bar{u}\gamma_\mu u - \frac{1}{3}\bar{d}\gamma_\mu d|p\rangle + \langle n|\frac{2}{3}\bar{u}\gamma_\mu u - \frac{1}{3}\bar{d}\gamma_\mu d|n\rangle \xrightarrow[p\leftrightarrow n]{u\leftrightarrow d} \frac{1}{3}\langle p|\bar{u}\gamma_\mu u + \bar{d}\gamma_\mu d|p\rangle. \quad (3)$$

We will use these relations to compare our lattice results, obtained for the isovector and isoscalar combinations, with the experimental data for the proton and neutron matrix elements.

We use the symmetrized lattice conserved vector current, $\mathcal{O}^V_\mu = \frac{1}{2}[j_\mu(x) + j_\mu(x-\hat{\mu})]$, with

$$j_\mu(x) = \frac{1}{2}[\bar{\psi}(x+\hat{\mu})U^\dagger_\mu(x)(1+\gamma_\mu)\tau_a\psi(x) - \bar{\psi}(x)U_\mu(x)(1-\gamma_\mu)\tau_a\psi(x+\hat{\mu})], \quad (4)$$

where $\bar{\psi} = (\bar{u}, \bar{d})$ and τ_a acts in flavor space. We consider $\tau_a = \tau_3$, the third Pauli matrix, for the isovector case, and $\tau_a = \mathbb{1}/3$ for the isoscalar case. $\hat{\mu}$ is the unit vector in direction μ and $U_\mu(x)$ is the gauge link connecting site x with $x+\hat{\mu}$. Using the conserved lattice current means that no renormalization of the vector operator is required.

The matrix element of the vector current can be decomposed in terms of the Dirac F_1 and Pauli F_2 form factors as

$$\Lambda^V_\mu(q^2) = \gamma_\mu F_1(q^2) + \frac{i\sigma_{\mu\nu}q^\nu}{2m_N}F_2(q^2). \quad (5)$$

F_1 and F_2 can also be expressed in terms of the nucleon electric G_E and magnetic G_M Sachs form factors via the relations

$$G_E(q^2) = F_1(q^2) + \frac{q^2}{(2m_N)^2}F_2(q^2), \quad \text{and}$$
$$G_M(q^2) = F_1(q^2) + F_2(q^2). \quad (6)$$

B. Lattice extraction of form factors

On the lattice, after Wick rotation to Euclidean time, extraction of matrix elements requires the calculation of a three-point correlation function shown schematically in Fig. 1. For simplicity we will take $x_0 = (\vec{0}, 0)$ from here on. We use sequential inversions through the sink, fixing the sink momentum $\vec{p}'$ to zero, which constrains $\vec{p} = -\vec{q}$:

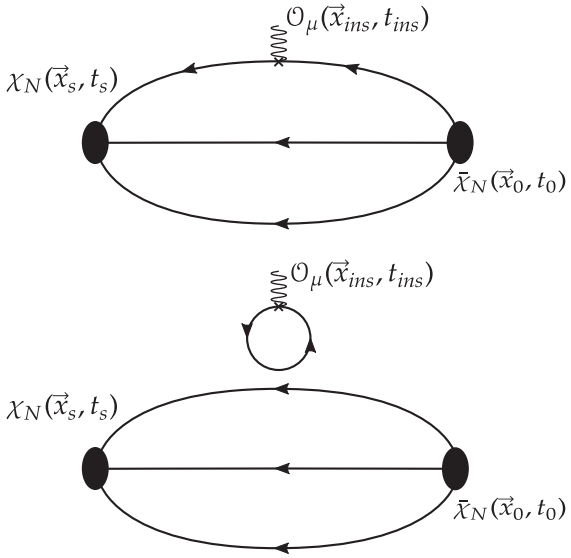

FIG. 1. Three-point nucleon correlation function with source at x_0, sink at x_s and current insertion $\mathcal{O}_\mu$ at x_{ins}. The connected contribution is shown in the upper panel and the disconnected contribution in the lower panel.

$$G_\mu(\Gamma;\vec{q};t_s,t_{\rm ins}) = \sum_{\vec{x}_s,\vec{x}_{\rm ins}} e^{-i\vec{q}.\vec{x}_{\rm ins}}\Gamma^{\alpha\beta}\langle\bar{\chi}_N^\beta(\vec{x}_s;t_s)|\times\mathcal{O}^\mu(\vec{x}_{\rm ins};t_{\rm ins})|\chi_N^\alpha(\vec{0};0)\rangle \xrightarrow[t_{\rm ins}\to\infty]{t_s-t_{\rm ins}\to\infty} \sum_{ss'}\Gamma^{\alpha\beta}\langle\chi_N^\beta|N(0,s')\rangle\times\langle N(p,s)|\bar{\chi}_N^\alpha\rangle\langle N(0,s')|\mathcal{O}_\mu(q)|N(p,s)\rangle\times e^{-E_N(\vec{p})t_{\rm ins}}e^{-m_N(t_s-t_{\rm ins})}, \quad (7)$$

where Γ is a matrix acting on Dirac indices α and β and χ_N is the standard nucleon interpolating operator given by

$$\chi_N^\alpha(\vec{x},t) = \epsilon^{abc}u_\alpha^a(x)[u^{b\intercal}(x)C\gamma_5 d^c(x)]. \quad (8)$$

with $C=\gamma_0\gamma_2$ the charge conjugation matrix. In the second line of Eq. (7), we have inserted twice a complete set of states with the quantum numbers of the nucleon, of which, after assuming large time separations, only the nucleon survives with higher energy states being exponentially suppressed. We use Gaussian smeared point-sources [8,9] to increase the overlap with the nucleon state with APE smearing applied to the gauge links, with the same parameters as in Ref. [10], tuned so as to yield a rms radius of about 0.5 fm. These are the same parameters as in Ref. [11], namely $(N_G,\alpha_G)=(50,4)$ for the Gaussian smearing and $(N_{\rm APE},\alpha_{\rm APE})=(50,0.5)$ for the APE smearing.

We construct an optimized ratio dividing G_μ by a combination of two-point functions. The optimized ratio R_μ is given by

$$R_\mu(\Gamma;\vec{q};t_s;t_{\rm ins}) = \frac{G_\mu(\Gamma;\vec{q};t_s;t_{\rm ins})}{G(\vec{0};t_s)}\left[\frac{G(\vec{0};t_s)G(\vec{q};t_s-t_{\rm ins})G(\vec{0};t_{\rm ins})}{G(\vec{q};t_s)G(\vec{0};t_s-t_{\rm ins})G(\vec{q};t_{\rm ins})}\right]^{\frac{1}{2}} \quad (9)$$

with the two-point function given by

$$G(\vec{p};t) = \sum_{\vec{x}} e^{-i\vec{p}\,\vec{x}}\Gamma_0^{\alpha\beta}\langle\bar{\chi}_N^\beta(\vec{x};t)|\chi_N^\alpha(\vec{0};0)\rangle. \quad (10)$$

Γ_0 is the unpolarized projector, $\Gamma_0=\frac{1+\gamma_0}{4}$. After taking the large time limit, unknown overlaps and energy exponentials cancel in the ratio, leading to the time-independent quantity $\Pi_\mu(\Gamma;\vec{q})$, defined via:

$$R_\mu(\Gamma;\vec{q};t_s;t_{\rm ins}) \xrightarrow[t_{\rm ins}\to\infty]{t_s-t_{\rm ins}\to\infty} \Pi_\mu(\Gamma;\vec{q}). \quad (11)$$

Having $\Pi_\mu(\Gamma;\vec{q})$, different combinations of current insertion directions (μ) and nucleon polarizations determined by Γ yield different expressions for the form factors [12,13]. Namely, we have

$$\Pi_0(\Gamma_0;\vec{q}) = \mathcal{C}\frac{E_N+m_N}{2m_N}G_E(Q^2),$$
$$\Pi_i(\Gamma_0;\vec{q}) = \mathcal{C}\frac{q_i}{2m_N}G_E(Q^2),$$
$$\Pi_i(\Gamma_k;\vec{q}) = \mathcal{C}\frac{\epsilon_{ijk}q_j}{2m_N}G_M(Q^2), \quad (12)$$

where $Q^2=-q^2$, is the Euclidean momentum transfer squared, $\mathcal{C}=\sqrt{\frac{2m_N^2}{E_N(E_N+m_N)}}$, and the polarized projector is given by $\Gamma_k=i\gamma_5\gamma_k\Gamma_0$, and $i,\ k=1,2,3$.

In what follows, we will use three methods to extract Π_μ from lattice data:

(i) *Plateau method*. We seek to identify a range of values of $t_{\rm ins}$ where the ratio R_μ is time-independent (plateau region). We fit, within this window, R_μ to a constant and use multiple t_s values. Excited states are considered suppressed when our result does not change with t_s.

(ii) *Two-state fit method*. We fit the time dependence of the three- and two-point functions keeping contributions up to the first excited state. Namely, we truncate the two-point function of Eq. (10) keeping only the ground and first excited states to obtain

$$G(\vec{p};t) = c_0(\vec{p})e^{-E(\vec{p})t}[1+c_1(\vec{p})e^{-\Delta E_1(\vec{p})t} + \mathcal{O}(e^{-\Delta E_2(\vec{p})t})]. \quad (13)$$

Similarly, the three-point function of Eq. (7) becomes

$$G_\mu(\Gamma;\vec{q};t_s,t_{\rm ins}) = a_{00}^\mu(\Gamma;\vec{q})e^{-m(t_s-t_{\rm ins})}e^{-E(\vec{q})t_{\rm ins}}\times[1+a_{01}^\mu(\Gamma;\vec{q})e^{-\Delta E_1(\vec{q})t_{\rm ins}} + a_{10}^\mu(\Gamma;\vec{q})e^{-\Delta m_1(t_s-t_{\rm ins})} + a_{11}^\mu(\Gamma;\vec{q})e^{-\Delta m_1(t_s-t_{\rm ins})}e^{-\Delta E_1(\vec{q})t_{\rm ins}} + \mathcal{O}[\min(e^{-\Delta m_2(t_s-t_{\rm ins})},e^{-\Delta E_2(\vec{q})t_{\rm ins}})]], \quad (14)$$

where $\Delta E_k(\vec{p})=E_k(\vec{p})-E(\vec{p})$ is the energy difference between the $k^{\rm th}$ nucleon excited state and the ground state at momentum $\vec{p}$ and $m=E(\vec{0})$ and $\Delta m_k=\Delta E_k(\vec{0})$. The desired ground state matrix element is given by

$$\Pi_\mu(\Gamma;\vec{q}) = \frac{a_{00}^\mu(\Gamma;\vec{q})}{\sqrt{c_0(\vec{0})c_0(\vec{q})}}. \quad (15)$$

In practice, we fit simultaneously the three-point function and the finite and zero momentum two-point functions in a twelve parameter fit to determine m, $E(\vec{q})$, Δm_1, $\Delta E_1(\vec{q})$, $c_0(\vec{q})$, $c_0(\vec{0})$, $c_1(\vec{q})$, $c_1(\vec{0})$, $a_{00}^\mu(\Gamma;\vec{q})$, $a_{01}^\mu(\Gamma;\vec{q})$, $a_{10}^\mu(\Gamma;\vec{q})$ and $a_{11}^\mu(\Gamma;\vec{q})$. The

two-point function is evaluated using the maximum statistics available at time separation $t_s/a = 18$.

(iii) *Summation method*. We sum the ratio of Eq. (9) over the insertion time-slices. From the expansion up to first excited state of Eq. (14) one sees that a geometric sum arises, which yields

$$\sum_{t_{\rm ins}=a}^{t_s-a} R_\mu(\Gamma;\vec{q};t_s;t_{\rm ins}) \xrightarrow{t_s\to\infty} c + \Pi_\mu(\Gamma;\vec{q})t_s + \mathcal{O}(t_s e^{-\Delta m_1 t_s}). \quad (16)$$

The summed ratio is then fitted to a linear form and the slope is taken as the desired matrix element. We note that, in quoting final results, we do not use the values extracted from summation method However, it does provide an additional consistency check for the plateau values.

C. Lattice setup

The simulation parameters of the ensemble we use are tabulated in Table I. We use an $N_f = 2$ ensemble of twisted mass fermion configurations with clover improvement with quarks tuned to maximal twist, yielding a pion mass of about 130 MeV. The lattice volume is $48^3 \times 96$ and the lattice spacing is determined at $a = 0.0938(3)$ fm yielding a physical box length of about 4.5 fm. The value of the lattice spacing is determined using the nucleon mass, as explained in Ref. [14]. Details of the simulation and first results using this ensemble were presented in Refs. [4,10].

The parameters used for the calculation of the correlation functions are given in Table II. We use increasing statistics with increasing sink-source separation so that statistical errors are kept approximately constant. Furthermore, as will be discussed in Sec. III, $G_E(Q^2)$ is found to be more susceptible to excited states compared to $G_M(Q^2)$, requiring larger separations for ensuring their suppression. Therefore, we carry out sequential inversions for five sink-source separations using the unpolarized projector Γ_0, which yields $G_E(Q^2)$ according Eq. (12). To obtain $G_M(Q^2)$, we carry out three additional sequential inversions, one for each polarized projector Γ_k, $k = 1, 2, 3$, for each of the three smallest separations.

TABLE I. Simulation parameters of the ensemble used in this calculation, first presented in Ref. [4]. The nucleon and pion mass and the lattice spacing have been determined in Ref. [14].

$\beta = 2.1$, $c_{\rm SW} = 1.57751$, $a = 0.0938(3)$ fm, $r_0/a = 5.32(5)$	
$48^3 \times 96$, $L = 4.5$ fm	$\alpha\mu = 0.0009$ $m_\pi = 0.1304(4)$ GeV $m_\pi L = 2.98(1)$ $m_N = 0.932(4)$ GeV

TABLE II. Parameters of the calculation of the form factors. The first column shows the sink-source separations used, the second column the sink projectors and the last column the total statistics ($N_{\rm st}$) obtained using $N_{\rm cnf}$ configurations times $N_{\rm src}$ source-positions per configuration.

t_s [a]	Proj.	$N_{\rm cnf} \cdot N_{\rm src} = N_{\rm st}$
10,12,14	Γ_0, Γ_k	$578 \cdot 16 = 9248$
16	Γ_0	$530 \cdot 88 = 46640$
18	Γ_0	$725 \cdot 88 = 63800$

III. RESULTS

A. Analysis

1. Isovector contributions

We use the three methods, described in the previous section, to analyze the contribution due to the excited states and extract the desired nucleon matrix element.

We demonstrate the quality of our data and two-state fits in Figs. 2 and 3 for the isovector contributions to $G_E(Q^2)$ and $G_M(Q^2)$, respectively, for three momentum transfers, namely the first, second and fourth nonzero Q^2 values of our setup. In these figures, we show the ratio after the appropriate combinations of Eq. (12) are taken to yield either $G_E^{u-d}(Q^2)$ or $G_M^{u-d}(Q^2)$. We indeed observe larger excited state contamination in the case of $G_E^{u-d}(Q^2)$, which is the reason for considering larger values of t_s for this case. We note that for fitting the plateau and summation methods, the ratios of Eq. (9) are constructed with two- and

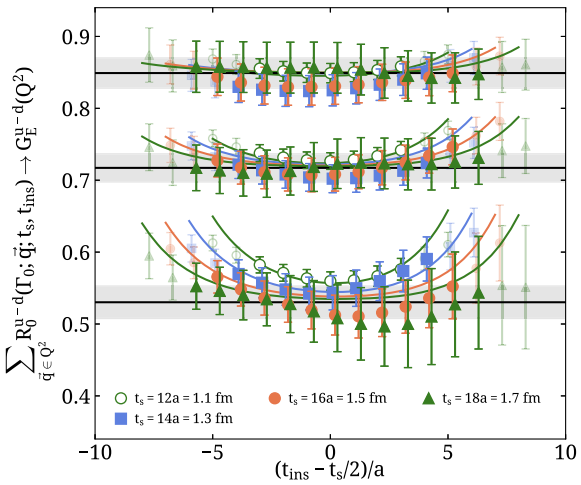

FIG. 2. Ratio yielding the isovector electric Sachs form factor. We show results for three representative Q^2 values, namely the first, second and fourth nonzero Q^2 values from top to bottom, for $t_s = 12a$ (open circles), $t_s = 14a$ (filled squares), $t_s = 16a$ (filled circles) and $t_s = 18a$ (filled triangles). The curves are the results from the two-state fits, with the fainter points excluded from the fit. The band is the form factor value extracted using the two-state fit.

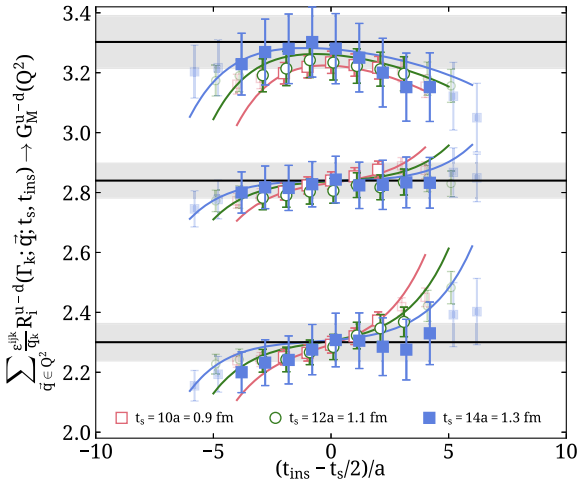

FIG. 3. Ratio yielding the isovector magnetic Sachs form factor. We show results for three representative Q^2 values, namely the first, second and fourth nonzero Q^2 values from top to bottom, for $t_s = 10a$ (open squares), $t_s = 12a$ (open circles), and $t_s = 14a$ (filled squares). The curves are the results from the two-state fits, with the fainter points excluded from the fit. The band is the form factor value extracted using the two-state fit.

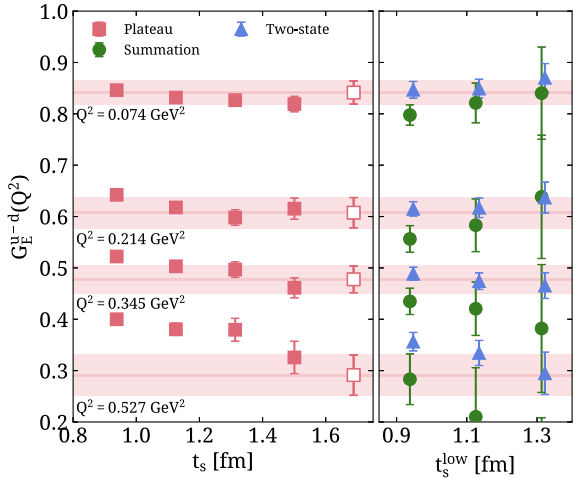

FIG. 4. Isovector electric form factor, for four nonzero Q^2 values, extracted from the plateau method (squares), the summation method (circles) and the two-state fit method (triangles). The plateau method results are plotted as a function of the sink-source separation while the summation and two-state fit results are plotted as a function of t_s^{low}, i.e. of the smallest sink-source separation included in the fit, with t_s^{high} kept fixed at $t_s = 18a = 1.7$ fm. The open square and band shows the selected value and its statistical error used to obtain our final results.

three-point functions with the same source positions and gauge configurations. For the two-state fit, as already mentioned, we use the two-point correlation function at the maximum statistics available, namely 725 configurations times 88 source positions, as indicated in Table II. These are the ratios shown in Figs. 2 and 3, which differ from those used for the plateau fits.

The investigation of excited states is facilitated further by Figs. 4 and 5. These plots indicate that excited state contributions are present in $G_E^{u-d}(Q^2)$ for the first three sink-source separations of $t_s/a = 10$, 12 and 14 in particular for larger momentum transfer. For the two larger sink-source separations we see convergence of the results extracted from the plateau method, which are in agreement with those from the summation method and the two-state fits when the lower fit range is $t_s^{\text{low}} = 12a = 1.1$ fm. For $G_M^{u-d}(Q^2)$, all results from the three sink-source separations are in agreement and consistent with the summation and two-state fit methods within their errors. The values obtained at $t_s = 18a = 1.7$ fm for the case of $G_E^{u-d}(Q^2)$ and $t_s = 14a = 1.3$ fm for the case of $G_M^{u-d}(Q^2)$ are shown in Figs. 4 and 5 with the open symbols and associated error band that demonstrates consistency with the values extracted using the summation and two-state fit methods.

Our results for the isovector electric Sachs form factor extracted using all available t_s values and from the summation and two-state fit methods are shown in Fig. 6. On the same plot we show the curve obtained from a parameterization of experimental data for $G_E^p(Q^2)$ and $G_E^n(Q^2)$ according to Ref. [15], using the parameters obtained in Ref. [16], and taking the isovector combination $G_E^p(Q^2) - G_E^n(Q^2)$. We see that as the sink-source separation is increased, our results tend towards the experimental curve. The results from the two-state fit method using $t_s^{\text{low}} = 1.1$ fm is consistent with those extracted from the plateau for $t_s = 1.7$ fm for all Q^2 values. Results extracted using the summation method are consistent within their large errors to those obtained from fitting the plateau for $t_s = 1.7$ fm.

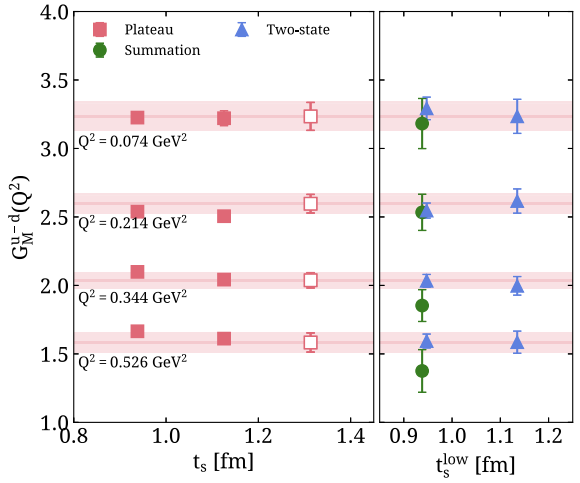

FIG. 5. Isovector magnetic form factor. The notation is the same as that in Fig. 4. For the summation and two-state fit methods, the largest sink-source separation included in the fit is kept fixed at $t_s^{\text{high}} = 14a = 1.3$ fm.

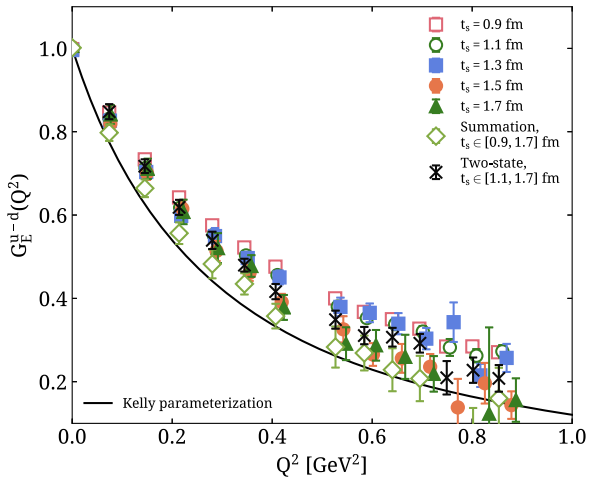

FIG. 6. Isovector electric Sachs form factor as a function of the momentum transfer squared (Q^2). Symbols for the plateau method follow the notation of Figs. 2 and 3. Results from the summation method are shown with open diamonds and for the two-state fit method with the crosses. The solid line shows $G_E^p(Q^2) - G_E^n(Q^2)$ using Kelly's parameterization of the experimental data [15] with parameters taken from Alberico *et al.* [16].

In Fig. 7, we show our results for the isovector magnetic form factor. We observe that excited state effects are milder than in the case of $G_E^{u-d}(Q^2)$, corroborating the conclusion drawn by observing Fig. 5. We also see agreement with the experimental curve for Q^2 values larger than ~0.2 GeV^2. However, our lattice results underestimate the experimental ones at the two lowest Q^2 values. Excited state effects are seen to be small for this quantity, and thus they are unlikely to be the cause of this discrepancy given the consistency of our results at three separations, as well as with those extracted using the summation and the two-state fit method. This small discrepancy could be due to suppressed pion

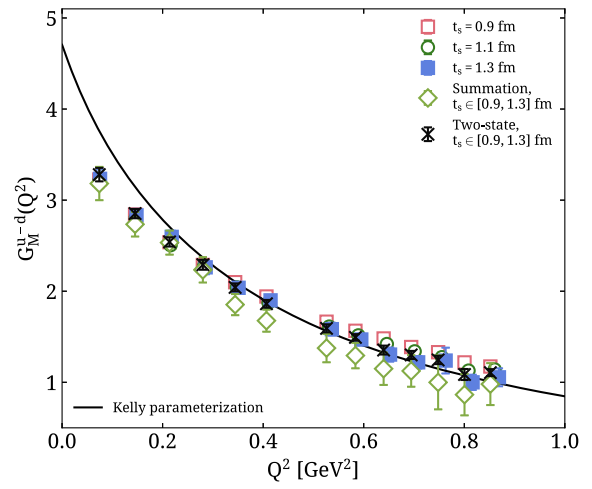

FIG. 7. Isovector magnetic Sachs form factor as a function of the momentum transfer squared. The notation is the same as that of Fig. 6.

cloud effects, due to the finite volume, that could be more significant at low momentum transfer. For example, a study of the magnetic dipole form factor G_{M1} in the $N \to \Delta$ transition using the Sato-Lee model predicts larger pion cloud contributions at low momentum transfer [17]. Lattice QCD computations also observe a discrepancy at lower Q^2 for G_{M1} when compared to experiment [18]. Analysis on a larger volume is ongoing to investigate volume effects not only in $G_M(Q^2)$ but also for other nucleon matrix elements and the results will be reported in subsequent publications. Our results for the form factors at all sink-source separations and using the summation and two-state fit methods are included in Appendix A in Tables VIII–XI. Preliminary results for the isovector electromagnetic form factors have been presented for this ensemble in Refs. [19,20].

2. Isoscalar contributions

We perform a similar analysis for the isoscalar contributions, denoted by $G_E^{u+d}(Q^2)$ and $G_M^{u+d}(Q^2)$. As mentioned, we use the combination $(u+d)/3$ in the matrix element for the isoscalar such that it yields $G_{E,M}^{u+d}(Q^2) = G_{E,M}^p(Q^2) + G_{E,M}^n(Q^2)$. Having also the isovector combination $G_{E,M}^{u-d}(Q^2) = G_{E,M}^p(Q^2) - G_{E,M}^n(Q^2)$ the individual proton and neutron form factors can be extracted. While isovector matrix elements receive no disconnected contributions since they cancel in the isospin limit, the isoscalar form factors do include disconnected fermion loops, shown schematically in Fig. 1. These disconnected contributions are included for the first time here at the physical point to obtain the isoscalar form factors.

The connected isoscalar three-point function is computed using the same procedure as in the isovector case. We show results for the connected contribution to $G_E^{u+d}(Q^2)$ and $G_M^{u+d}(Q^2)$ in Figs. 8 and 9, respectively. These results are for the same momentum transfer values as used in Figs. 4 and 5. In the case of the isoscalar electric form factor, we observe contributions due to excited states that are similar to those observed for the isovector case. Namely, we find that a separation of about $t_s = 1.7$ fm is required for their suppression. For the isoscalar magnetic form factor, we observe that the values extracted from fitting the plateau at time separations $t_s = 1.1$ fm and $t_s = 1.3$ fm are consistent and also in agreement with the values extracted using the two-state fit and summation methods.

The disconnected diagrams of the electromagnetic form factors are particularly susceptible to statistical fluctuations, even at larger pion masses of 370 MeV as reported in Refs. [21,22]. Here we show results, at the physical pion mass, for the disconnected contribution to $G_E^{u+d}(Q^2)$ and $G_M^{u+d}(Q^2)$ in Fig. 10 for the first nonzero momentum transfer. The results are obtained using the same ensemble used for the connected contributions, detailed in Table I, using 2120 configurations, with two-point functions computed on 100 randomly chosen source positions per

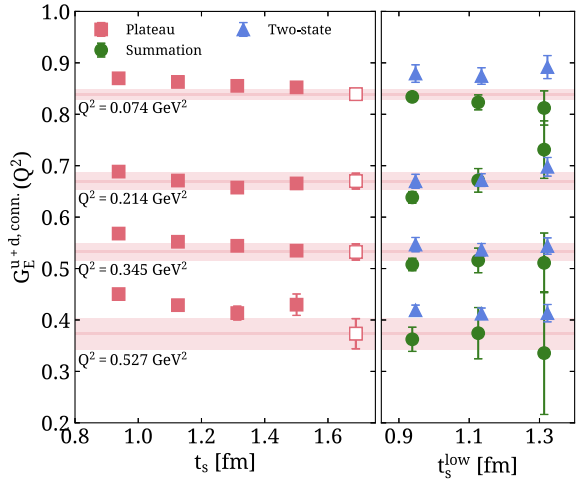

FIG. 8. Connected contribution to the $G_E^{u+d}(Q^2)$ form factor, for four nonzero Q^2 values, extracted from the plateau method (squares), the summation method (filled circles) and the two-state fit method (filled triangles). The notation is the same as in Fig. 4.

configuration. 2250 stochastic noise vectors are used for estimating the fermion loop. Averaging the proton and neutron two-point functions and the forward and backwards propagating nucleons yields a total of 8×10^5 statistics. More details of this calculation are presented in Ref. [23], where results for the axial form factors are shown.

In the case of the electric form factor, we obtain $G_E^{u+d,\mathrm{disc}}(Q^2 = 0.074\ \mathrm{GeV}^2) = -0.002(3)$, which is consistent with zero and about 0.2% of the value of the connected contribution and four times smaller than its statistical error. For the magnetic form factor, fitting to the plateau we obtain $G_M^{u+d,\mathrm{disc}}(Q^2 = 0.074\ \mathrm{GeV}^2) = -0.016(7)$ which is 2% of the value of the connected contribution at this Q^2 and half the value of the statistical

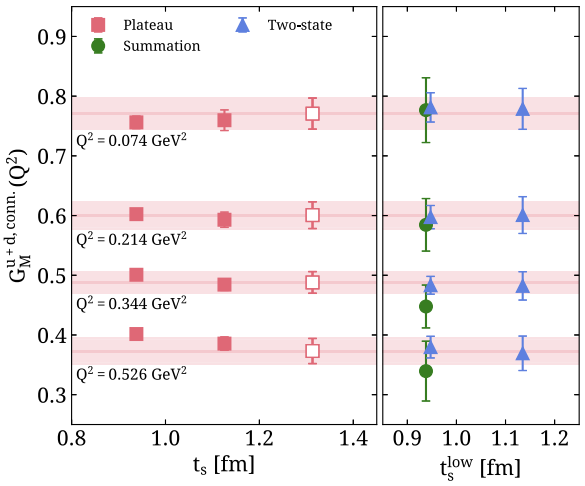

FIG. 9. Connected contribution to the $G_M^{u+d}(Q^2)$ form factor. The notation is the same as in Fig. 5.

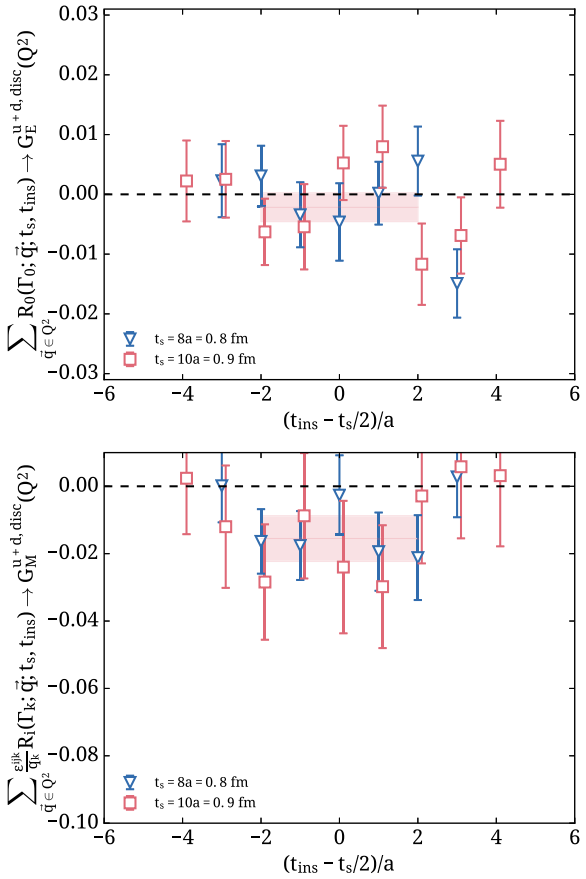

FIG. 10. Disconnected contribution to the electric (upper panel) and magnetic (lower panel) isoscalar Sachs form factors for sink-source separation $t_s = 8a = 0.75$ fm (inverted triangles) and $t_s = 10a = 0.94$ fm (squares) for the first nonzero momentum transfer of $Q^2 = 0.074\ \mathrm{GeV}^2$. The horizontal bands show the values obtained after fitting with the plateau method to the results at $t_s = 10a = 0.94$ fm.

error. These values are consistent with a dedicated study of the disconnected contributions using an ensemble of clover fermions with pion mass of 317 MeV [24] and a recent result at the physical point presented in Ref. [25]. There it was shown that $G_M^{u+d,\mathrm{disc}}(Q^2)$ is negative and largest in magnitude at $Q^2 = 0$ while $G_E^{u+d,\mathrm{disc}}(Q^2)$ is largest at around $Q^2 = 0.4\ \mathrm{GeV}^2$. In our case, at our largest momentum transfer, we find $G_E^{u+d,\mathrm{disc}}(Q^2 = 0.280\ \mathrm{GeV}^2) = -0.0056(40)$, which is 1% of the value of the connected contribution at this momentum transfer and smaller than the associated statistical error. Investigation of methods for increasing the precision at the physical point is ongoing, with preliminary results presented in Ref. [26] for the ensemble used here, and will be reported in a separate work.

We show our results for the connected contribution to the isoscalar electric and magnetic form factors in Figs. 11 and 12 extracted from the plateau method for all available sink-source separations, and from the

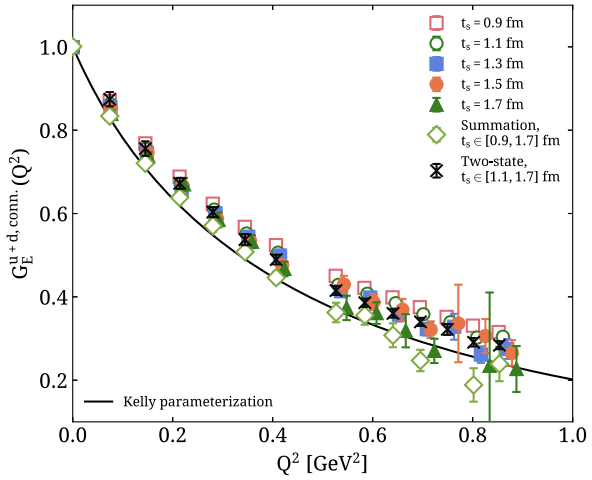

FIG. 11. Connected contribution to the isoscalar electric Sachs form factor as a function of the momentum transfer, using the notation of Fig. 11. The solid line shows $G_E^p(Q^2) + G_E^n(Q^2)$ using the Kelly parameterization of experimental data from Ref. [15] with parameters taken from Alberico *et al.* [16].

summation and the two-state fit methods. The isoscalar electric form factor tends to decrease as the sink-source separation increases approaching the experimental parameterization. This may indicate residual excited state effects, that need to be further investigated by going to larger time separations. For the isoscalar magnetic form factor, we observe a weaker dependence on t_s pointing to less severe excited state effects.

B. Q^2 dependence of the form factors

1. Isovector and isoscalar form factors

We fit $G_E(Q^2)$ and $G_M(Q^2)$ to both a dipole ansatz and the z-expansion form. The truncated z expansion is

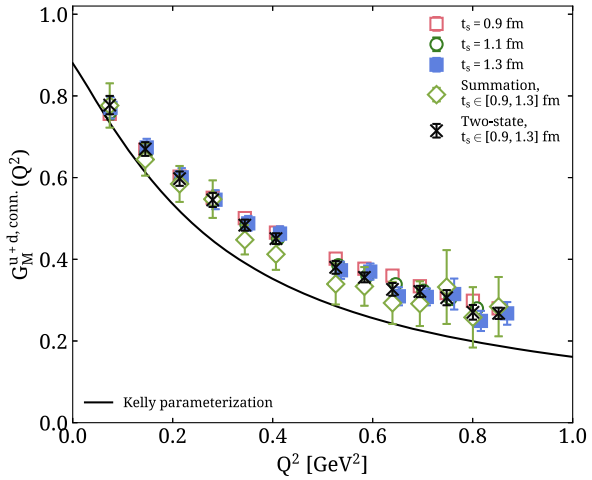

FIG. 12. Connected contribution to the isoscalar magnetic Sachs form factor as a function of the momentum transfer. The notation is the same as in Fig. 11.

expected to model better the low-Q^2 [7] dependence of the form factors, while the dipole form is motivated by vector-meson pole contributions to the form factors [27]. For the case of the dipole fits, we use

$$G_i(Q^2) = \frac{G_i(0)}{(1 + \frac{Q^2}{M_i^2})^2}, \tag{17}$$

with $i = E, M$, allowing both $G_M(0)$ and M_M to vary for the case of magnetic form factor, while constraining $G_E(0) = 1$ for the case of the electric form factor. For the z expansion, we use the form [7]

$$G_i(Q^2) = \sum_{k=0}^{k_{\max}} a_k^i z^k, \quad \text{where } z = \frac{\sqrt{t_{\text{cut}} + Q^2} - \sqrt{t_{\text{cut}}}}{\sqrt{t_{\text{cut}} + Q^2} + \sqrt{t_{\text{cut}}}} \tag{18}$$

and take $t_{\text{cut}} = 4m_\pi^2$. For both isovector and isoscalar $G_E(Q^2)$ we fix $a_0^E = 1$ while for $G_M(Q^2)$ we allow all parameters to vary. We use Gaussian priors for a_k^i for $k \geq 2$ with width $w = 5\max(|a_0^i|, |a_1^i|)$ as proposed in Ref. [28]. We observe larger errors when fitting with the z expansion compared to the dipole form. In Fig. 13, we show a_0^M and a_1^M from fits to the magnetic isovector form factor and a_1^E from fits to the electric as a function of $k_{\max}$ and observe no significant change in the fitted parameters beyond $k_{\max} \geq 2$. We also note that the resulting values for a_k^i for $k \geq 2$ obtained are well within the Gaussian priors, i.e. $|a_k^i| \ll 5\max(|a_0^i|, |a_1^i|)$. We, therefore, quote results using $k_{\max} = 2$ from here on.

Fits to the Q^2 dependence of $G_E^{u-d}(Q^2)$ are shown in Fig. 14 using the values extracted from the plateau at $t_s = 18a = 1.7$ fm. The line and error band are the result of fitting to either dipole or the z expansion for all available Q^2 values. Both the dipole and z-expansion form describe the lattice QCD results well. In this plot, we also show results from experiment, using data for $G_E^p(Q^2)$ obtained

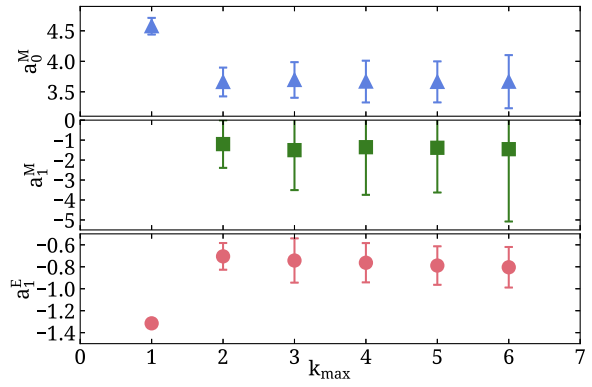

FIG. 13. Results from fitting using the z expansion as a function of $k_{\max}$ for a_1^E (lower panel), a_1^M (center panel) and a_0^M (top panel) of Eq. (18).

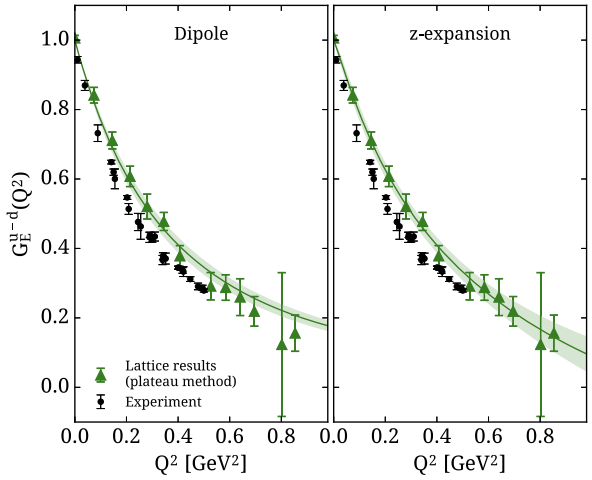

FIG. 14. Isovector electric Sachs form factor as a function of the momentum transfer extracted from the plateau method at $t_s = 18a = 1.7$ fm (triangles). We show fits using the dipole form (left) and the z expansion (right). The black points are obtained using experimental data for $G_E^p(Q^2)$ from Ref. [29] and for $G_E^n(Q^2)$ from Refs. [30–44].

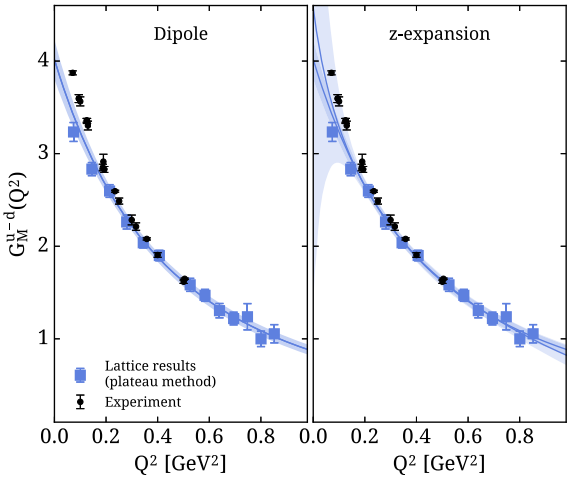

FIG. 15. Isovector magnetic Sachs form factor as a function of the momentum transfer extracted from the plateau method at $t_s = 14a = 1.3$ fm (squares). We show fits using the dipole form (left) and the z expansion (right). The smaller error band corresponds to fitting to all Q^2 values, while the larger band is obtained after omitting the two smallest values. The black points are obtained using experimental data for $G_M^p(Q^2)$ from Ref. [29] and for $G_M^n(Q^2)$ from Refs. [45–50].

from Ref. [29] and data for $G_E^n(Q^2)$ from Refs. [30–44]. To subtract the two form factors and obtain the isovector combination, we linearly interpolate the more accurate experimental data of $G_E^p(Q^2)$ to the Q^2 values for which $G_E^n(Q^2)$ is available.

For both the dipole and z-expansion fit, the resulting curve lies about one standard deviation above the experimental data. This small discrepancy may be due to small residual excited state effects, which would require significant increase of statistics at larger sink-source separations to identify. Having only performed the calculation using one ensemble we cannot check directly for finite volume and cutoff effects. However, in a previous study employing $N_f = 2$ twisted mass fermions at heavier than physical pion masses and three values of the lattice spacing, we found no detectable cutoff effects in these quantities for a lattice spacing similar to the one used here [13]. We have also performed a volume assessment using the aforementioned heavier mass twisted mass ensembles with $m_\pi L$ values ranging from 3.27 to 5.28. Namely, we found no volume dependence within our statistical accuracy between two ensembles with $m_\pi L = 3.27$ and $m_\pi L = 4.28$, respectively, and similar pion mass of $m_\pi \simeq 300$ MeV. We plan to carry out a high accuracy analysis of the volume dependence at the physical point on a lattice size of $64^3 \times 128$ keeping the other parameters fixed in a forthcoming publication.

The same analysis carried out for $G_E^{u-d}(Q^2)$ is also performed for $G_M^{u-d}(Q^2)$ in Fig. 15, where we use the result from fitting to the plateau at the largest sink-source separation available, namely $t_s = 14a = 1.3$ fm. As for the case of $G_E^{u-d}(Q^2)$, both the dipole ansatz and z expansion describe well the lattice QCD data. The plots show two bands, one when including all Q^2 values, resulting in the smaller error band, and one in which the first two Q^2 values are omitted, resulting in the larger band. The experimental data shown are obtained using $G_M^p(Q^2)$ from the same experiment as for $G_E^p(Q^2)$ shown in Fig. 14, namely Ref. [29], and $G_M^n(Q^2)$ from Refs. [45–50].

In both the dipole and z-expansion fits of $G_M^{u-d}(Q^2)$, we find that the Q^2 dependence is consistent with experiment after $Q^2 \simeq 0.2$ GeV^2. We suspect that the deviation at the two smallest Q^2 values is due to finite volume effects. As already mentioned, we plan to further investigate this using an ensemble of $N_f = 2$ twisted mass fermions on a larger volume of $64^3 \times 128$. As can be seen, discarding the two lowest Q^2 values results in a larger error for $G_M^{u-d}(0)$, in particular in the case of the z expansion.

We show the momentum dependence of the disconnected contribution to $G_M^{u+d}(Q^2)$ in Fig. 16. The large errors do not permit as thorough analysis as for the connected contribution. Since the disconnected isoscalar contributions do not follow a dipole form, and in the absence of any theoretically motivated form for the disconnected contributions, we use a z-expansion fit with $k_{\max} = 2$, fixing $a_0 = 0$ for $G_E^{u+d,\mathrm{disc}}(Q^2)$ and with $k_{\max} = 1$, allowing both a_0 and a_1 to vary. For the case of $G_E^{u+d,\mathrm{disc}}(Q^2)$ we find results consistent with zero. For the magnetic case, the disconnected contribution decreases the form factor by at most 3% at $Q^2 = 0$.

We add connected and disconnected contributions to obtain the isoscalar contributions shown in Figs. 17 and 18. There are small discrepancies between our lattice data and

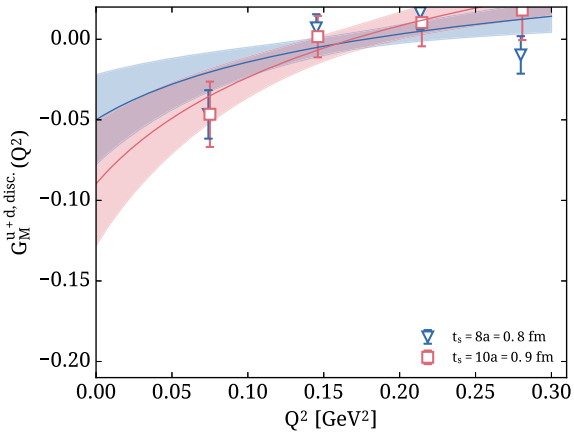

FIG. 16. Disconnected contribution to the isoscalar magnetic Sachs form factor as a function of the momentum transfer for $t_s = 8a = 0.7$ fm (inverted triangles) and $t_s = 10a = 0.9$ fm (squares). The bands show fits to the z-expansion form with $k_{\max} = 1$.

experiment at larger Q^2 values. Whether these are due to volume effects or other lattice artifacts will be investigated in a follow-up study.

The slope of the form factors at $Q^2 = 0$ is related to the isovector electric and magnetic radius as follows,

$$\frac{\partial}{\partial Q^2} G_i(Q^2)|_{Q^2=0} = -\frac{1}{6} G_i(0) \langle r_i^2 \rangle, \tag{19}$$

with $i = E, M$ for the electric and magnetic form factors, respectively. For the z expansion, this is given by

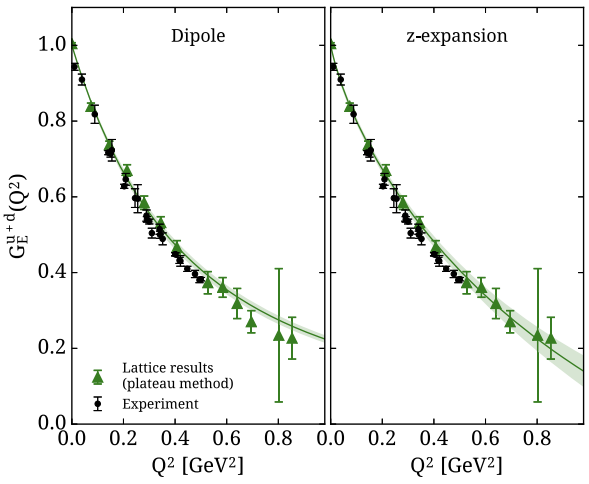

FIG. 17. Isoscalar electric Sachs form factor with fits to the dipole form (left) and to the z expansion (right). We show with triangles the sum of connected and disconnected contributions, with the plateau result for $t_s = 18a = 1.7$ fm for the connected and for $t_s = 10a = 0.9$ fm for the disconnected. The black points show experiment using the same data as for Fig. 14.

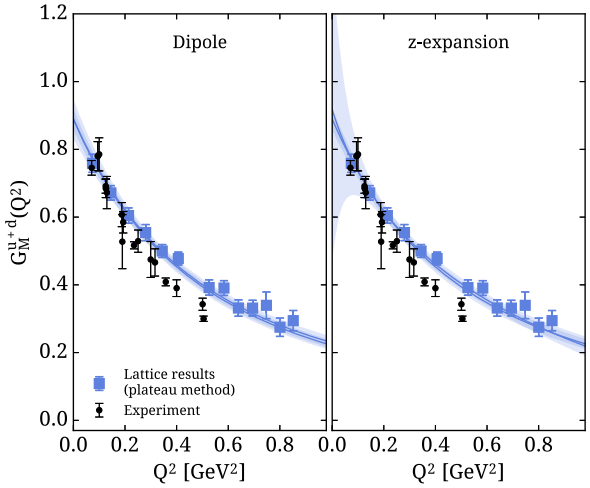

FIG. 18. Isoscalar magnetic Sachs form factor with fits to the dipole form (left) and to the z expansion (right). We show with triangles the sum of connected and disconnected contributions, with the plateau result for $t_s = 14a = 1.3$ fm for the connected and for $t_s = 10a = 0.9$ fm for the disconnected. The black points show experiment using the same data as for Fig. 15.

$$\langle r_i^2 \rangle = -\frac{6}{4t_{\text{cut}}} \frac{a_1^i}{a_0^i} \tag{20}$$

and for the dipole fit

$$\langle r_i^2 \rangle = \frac{12}{M_i^2}. \tag{21}$$

Furthermore, the nucleon magnetic moment is defined as $\mu = G_M(0)$ and is obtained directly from the fitted parameter in both cases. As for the form factors, we will denote the isovector radii and magnetic moment with the $u-d$ superscript and for the isoscalar with $u+d$. We tabulate our results for the isovector radii and magnetic moment from both the dipole and z-expansion fits in Tables III and

TABLE III. Results for the isovector electric charge radius of the nucleon ($\langle r_E^2 \rangle^{u-d}$) from fits to $G_E^{u-d}(Q^2)$. In the first column, we show t_s for the plateau method and the t_s fit range for the summation and two-state fit methods.

	Dipole		z expansion	
t_s [fm]	$\langle r_E^2 \rangle^{u-d}$ [fm^2]	$\frac{\chi^2}{\text{dof}}$	$\langle r_E^2 \rangle^{u-d}$ [fm^2]	$\frac{\chi^2}{\text{dof}}$
		Plateau		
0.94	0.523(08)	2.0	0.562(19)	1.2
1.13	0.562(14)	1.9	0.677(37)	0.7
1.31	0.580(26)	1.2	0.718(75)	0.7
1.50	0.666(33)	0.9	0.61(10)	0.3
1.69	0.653(48)	0.6	0.52(14)	0.2
		Summation		
0.9–1.7	0.744(55)	0.3	0.79(14)	0.2
		Two-state		
1.1–1.7	0.623(33)	1.0	0.56(10)	0.8

TABLE IV. Results for the isovector magnetic charge radius of the nucleon ($\langle r_M^2\rangle^{u-d}$) and the isovector magnetic moment $G_M(0) = \mu^{u-d}$ from fits to $G_M^{u-d}(Q^2)$. In the first column, we show t_s for the plateau method and the t_s fit range for the summation and two-state fit methods. The two smallest Q^2 values are omitted from the fit.

	Dipole		z expansion	
t_s [fm]	$\langle r_M^2\rangle^{u-d}$ [fm^2]	$\frac{\chi^2}{\text{d.o.f}}$	$\langle r_M^2\rangle^{u-d}$ [fm^2]	$\frac{\chi^2}{\text{d.o.f}}$
		Plateau		
0.94	0.404(10)	0.3	0.59(13)	0.3
1.13	0.434(22)	0.3	0.82(23)	0.3
1.31	0.536(52)	0.3	0.79(40)	0.3
		Summation		
0.9-1.3	68(16)	0.1	1.83(49)	0.1
		Two-state		
0.9-1.3	0.470(31)	0.3	1.15(25)	0.3

	Dipole		z expansion	
t_s [fm]	$G_M^{u-d}(0)$	$\frac{\chi^2}{\text{d.o.f}}$	$G_M^{u-d}(0)$	$\frac{\chi^2}{\text{d.o.f}}$
		Plateau		
0.94	3.548(52)	0.3	3.85(16)	0.3
1.13	3.595(90)	0.3	4.13(31)	0.3
1.31	4.02(21)	0.3	4.31(57)	0.3
		Summation		
0.9-1.3	4.32(57)	0.1	6.35(1.35)	0.1
		Two-state		
0.9-1.3	3.74(14)	0.3	4.71(42)	0.3

IV, and from fits to the isoscalar form factors in Tables V and VI. For the isoscalar results shown in Tables V and VI, we show two results for each case, namely the result of fitting only the connected contribution in the first column of each case and the total contribution, by combining connected and disconnected, in the second column.

TABLE V. Results for the isoscalar electric charge radius of the nucleon ($\langle r_E^2\rangle^{u+d}$). In the first column, we show t_s for the plateau method and the t_s fit range for the summation and two-state fit methods. For each t_s and for each fit ansatz, we give the result from fitting to the connected contribution in the first column and to the total contribution of connected plus disconnected in the second column.

	Dipole $\langle r_E^2\rangle^{u+d}$ [fm^2]			z expansion $\langle r_E^2\rangle^{u+d}$ [fm^2]		
t_s [fm]	Connected	Total	$\frac{\chi^2}{\text{d.o.f}}$	Connected	Total	$\frac{\chi^2}{\text{d.o.f}}$
			Plateau			
0.94	0.440(3)	0.449(49)	4.5	0.418(9)	0.427(49)	0.9
1.13	0.469(6)	0.478(49)	1.9	0.464(17)	0.474(52)	0.7
1.31	0.494(12)	0.503(50)	0.9	0.485(34)	0.495(59)	0.5
1.50	0.502(14)	0.512(50)	0.3	0.494(41)	0.503(63)	0.4
1.69	0.527(22)	0.537(53)	0.9	0.493(60)	0.503(77)	0.8
			Summation			
0.9–1.7	0.565(20)	0.576(53)	0.9	0.555(54)	0.564(72)	0.6
			Two-state			
1.1–1.7	0.490(16)	0.499(51)	0.5	0.453(77)	0.462(91)	0.7

TABLE VI. Results for the isoscalar magnetic charge radius of the nucleon ($\langle r_M^2\rangle^{u+d}$) and the isoscalar magnetic moment $G_M^{u+d}(0)$. The notation is as in Table V.

	Dipole $\langle r_M^2\rangle^{u+d}$ [fm^2]			z expansion $\langle r_M^2\rangle^{u+d}$ [fm^2]		
t_s [fm]	Connected	Total	$\frac{\chi^2}{\text{d.o.f}}$	Connected	Total	$\frac{\chi^2}{\text{d.o.f}}$
			Plateau			
0.94	0.392(13)	0.302(34)	0.2	0.41(19)	0.32(20)	0.2
1.13	0.419(29)	0.329(47)	0.1	0.84(28)	0.78(32)	0.1
1.31	0.476(59)	0.394(82)	0.4	0.4(1.0)	0.4(1.1)	0.5
			Summation			
0.9–1.3	0.50(18)	0.42(24)	0.2	1.94(92)	2.0(1.3)	0.2
			Two-state			
0.9–1.3	0.439(44)	0.353(65)	0.2	0.89(47)	0.83(52)	0.2

	Dipole $G_M^{u+d}(0)$			z expansion $G_M^{u+d}(0)$		
t_s [fm]	Connected	Total	$\frac{\chi^2}{\text{d.o.f}}$	Connected	Total	$\frac{\chi^2}{\text{d.o.f}}$
			Plateau			
0.94	0.838(16)	0.808(18)	0.2	0.867(50)	0.837(50)	0.2
1.13	0.841(29)	0.811(30)	0.1	0.981(90)	0.951(90)	0.1
1.31	0.900(59)	0.870(60)	0.4	0.90(19)	0.87(19)	0.5
			Summation			
0.9–1.3	0.88(16)	0.85(16)	0.2	1.51(45)	1.48(45)	0.2
			Two-state			
0.9–1.3	0.861(47)	0.831(48)	0.2	1.01(14)	0.98(14)	0.2

For our final result for the isovector electric charge radius, we use the central value and statistical error of the result from the plateau method at $t_s = 18a = 1.7$ fm using a dipole fit to all Q^2 values. We also include a systematic error from the difference of the central values when comparing with the two-state fit method to account for excited states effects. Similarly, for the magnetic radius and moment, we take the result from the dipole fits to our largest sink-source separation, which for this case is $t_s = 14a = 1.31$ fm and as in the case of the electric charge radius, we take the difference with the two-state fit method as an additional systematic error. In this case, the values at the two lowest momenta are not included in the fit. Our final values for the isovector radii and isovector nucleon magnetic moment are:

$$\begin{aligned}\langle r_E^2\rangle^{u-d} &= 0.653(48)(30)\ \text{fm}^2,\\ \langle r_M^2\rangle^{u-d} &= 0.536(52)(66)\ \text{fm}^2, \quad \text{and}\\ \mu^{u-d} &= 4.02(21)(28),\end{aligned} \tag{22}$$

where the first error is statistical and the second error is a systematic obtained when comparing the plateau method to the two-state fit method as a measure of excited state effects. For the isoscalar radii and moment we follow a

similar analysis after adding the disconnected contribution from the plateau method for $t_s = 10a = 0.9$ fm. We obtain

$$\begin{aligned}\langle r_E^2\rangle^{u+d} &= 0.537(53)(38)\ \text{fm}^2,\\ \langle r_M^2\rangle^{u+d} &= 0.394(82)(42)\ \text{fm}^2, \quad \text{and}\\ \mu^{u+d} &= 0.870(60)(39).\end{aligned} \tag{23}$$

C. Proton and neutron form factors

Having the isovector and isoscalar contributions to the form factors, we can obtain the proton ($G^p(Q^2)$) and neutron ($G^n(Q^2)$) form factors via linear combinations taken from Eqs. (2) and (3) assuming isospin symmetry between up and down quarks and proton and neutron. Namely, we have:

$$\begin{aligned}G^p(Q^2) &= \frac{1}{2}[G^{u+d}(Q^2) + G^{u-d}(Q^2)]\\ G^n(Q^2) &= \frac{1}{2}[G^{u+d}(Q^2) - G^{u-d}(Q^2)]\end{aligned} \tag{24}$$

where $G^p(Q^2)$ ($G^n(Q^2)$) is either the electric or magnetic proton (neutron) form factor. In Figs. 19 and 20, we show results for the proton electric and magnetic Sachs form factors, respectively. As for the isoscalar case, the disconnected contributions have been included. The bands are from fits to the dipole form of Eq. (17). In these plots, we compare to experimental results from the A1 collaboration [29]. We observe a similar behavior when comparing to experiment as for the case of the isovector form factors. Namely, the dipole fit to the lattice data has a smaller slope for small values of Q^2 as compared to experiment, while

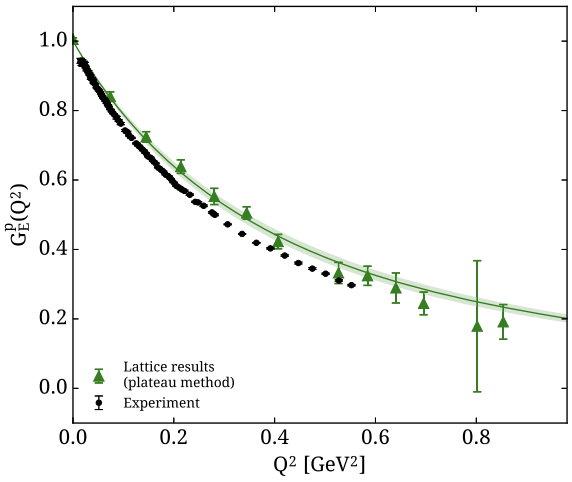

FIG. 19. Proton electric Sachs form factor as a function of the momentum transfer. We show with triangles the sum of connected and disconnected contributions, with the plateau result for $t_s = 18a = 1.7$ fm for the connected and for $t_s = 10a = 0.9$ fm for the disconnected. The band is a fit to the dipole form. The black points show experimental data from Ref. [29].

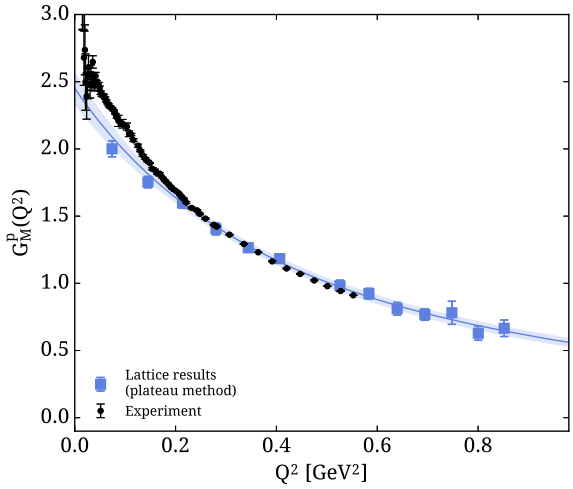

FIG. 20. Proton magnetic Sachs form factor as a function of the momentum transfer. We show with squares the sum of connected and disconnected contributions, with the plateau result for $t_s = 14a = 1.3$ fm for the connected and for $t_s = 10a = 0.9$ fm for the disconnected. The band is a fit to the dipole form. The black points show experimental data from Ref. [29].

$G_M^p(Q^2)$ reproduces the experimental momentum dependence for $Q^2 > 0.2$ GeV^2.

In Figs. 21 and 22, we show the same for the neutron form factors. For the neutron electric form factor we fit to the form [15]:

$$G_E^n(Q^2) = \frac{\tau A}{1+\tau B}\frac{1}{(1+\frac{Q^2}{\Lambda^2})^2} \tag{25}$$

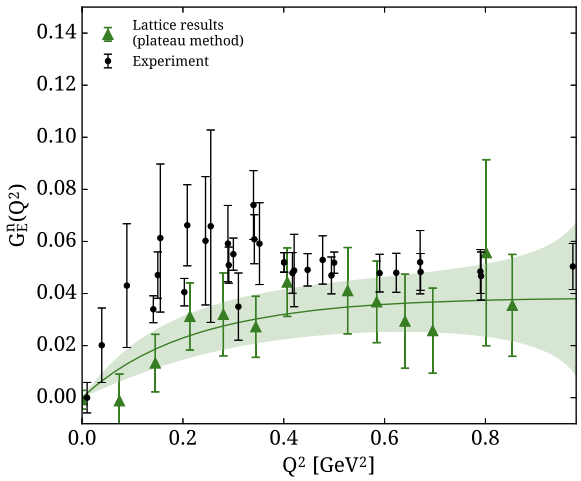

FIG. 21. Neutron electric Sachs form factor as a function of the momentum transfer. Triangles are from the sum of connected and disconnected contributions, with the plateau result for $t_s = 18a = 1.7$ fm for the connected and for $t_s = 10a = 0.9$ fm for the disconnected. The band is a fit to the form of Eq. (25). Experimental data are shown with the black points, obtained from Refs. [30–44].

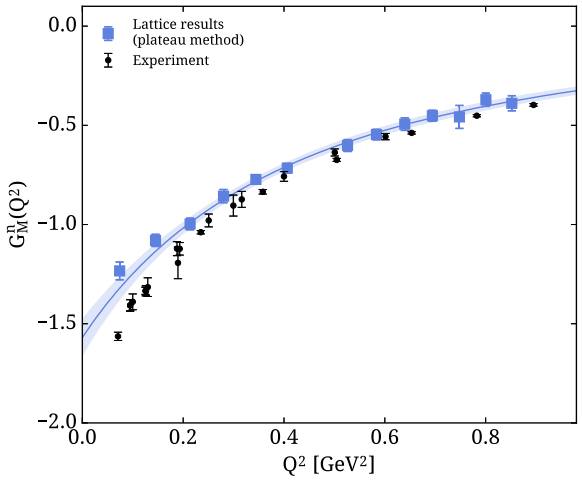

FIG. 22. Neutron magnetic Sachs form factor as a function of the momentum transfer. We show with squares the sum of connected and disconnected contributions, with the plateau result for $t_s = 14a = 1.3$ fm for the connected and for $t_s = 10a = 0.9$ fm for the disconnected. The band is a fit to the dipole form. The black points show experimental data from Refs. [45–50].

with $\tau = Q^2/(2m_N)^2$ and $\Lambda^2 = 0.71$ GeV^2 and allow A and B to vary. This ansatz reproduces our data well. We compare to a collection of experimental data from Refs. [30–44]. For $G_M^n(Q^2)$, we agree with the experimental data for $Q^2 > 0.2$ GeV^2, however we underestimate the magnetic moment by about 20%. Experimental data for $G_M^n(Q^2)$ shown in Fig. 22 are taken from Refs. [45–50].

We use Eq. (19) to obtain the radii using the dipole fits. For the case of $G_E^n(Q^2)$, the neutron electric radius is obtained via: $\langle r_E^2\rangle^n = -\frac{3A}{2m_N^2}$, where A is the parameter of Eq. (25). In all cases, we have combined connected and disconnected. We obtain:

$$\begin{aligned} \langle r_E^2\rangle^p &= 0.589(39)(33)\ \text{fm}^2, \\ \langle r_M^2\rangle^p &= 0.506(51)(42)\ \text{fm}^2, \quad \text{and} \\ \mu_p &= 2.44(13)(14), \end{aligned} \tag{26}$$

for the proton, and:

$$\begin{aligned} \langle r_E^2\rangle^n &= -0.038(34)(6)\ \text{fm}^2, \\ \langle r_M^2\rangle^n &= 0.586(58)(75)\ \text{fm}^2, \quad \text{and} \\ \mu_n &= -1.58(9)(12), \end{aligned} \tag{27}$$

for the neutron, where as in the case of the isoscalar and isovector, the first error is statistical and the second is a systematic obtained when comparing the plateau method to the two-state fit method as a measure of excited state effects.

IV. COMPARISON WITH OTHER RESULTS

A. Comparison of isovector and isoscalar form factors

Recent lattice calculations for the electromagnetic form factors of the nucleon include an analysis from the Mainz group [51] using $N_f = 2$ clover fermions down to a pion mass of 193 MeV, results from the PNDME collaboration [52] using clover valence fermions on $N_f = 2+1+1$ HISQ sea quarks down to pion mass of ∼220 MeV and $N_f = 2+1+1$ results from the ETM collaboration down to 213 MeV pion mass [53]. Simulations directly at the physical point have only been possible recently. The LHPC has published results in Ref. [54] using $N_f = 2+1$ HEX smeared clover fermions, which include an ensemble with $m_\pi = 149$ MeV. Preliminary results for electromagnetic nucleon form factors at physical or near physical pion masses have also been reported by the PNDME collaboration in Ref. [55] using clover valence quarks on HISQ sea quarks at a pion mass of 130 MeV and by the RBC/UKQCD collaboration using Domain Wall fermions at $m_\pi = 172$ MeV in Ref. [56].

In Fig. 23, we compare our results for $G_E^{u-d}(Q^2)$ from the plateau method using $t_s = 18a = 1.7$ fm to published results. We show results from Ref. [54] extracted from the summation method using three sink-source separations from 0.93 to 1.39 fm for their ensemble at the near-physical pion mass of $m_\pi = 149$ MeV. We note that their statistics of 7752 are about six times less than ours at the sink-source separation we use in this plot (see Table II).

In Fig. 24, we plot our results for $G_M^{u-d}(Q^2)$ from the plateau method using $t_s = 14a = 1.3$ fm and compare to those from LHPC. At this sink-source separation the statistics are similar, namely 7752 for the LHPC data and 9248 for the results from this work, however their errors are larger, possibly due to the fact that the summation

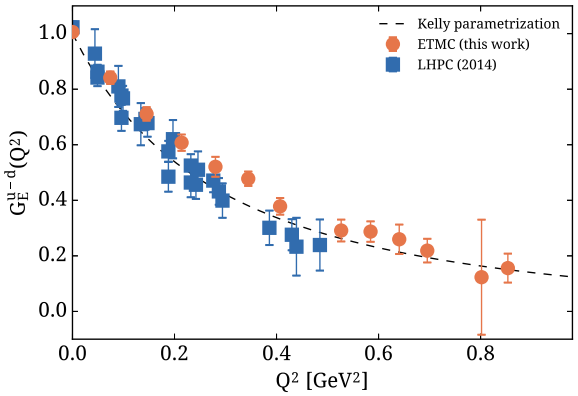

FIG. 23. Comparison of $G_E^{u-d}(Q^2)$ between results from this work (circles) denoted by ETMC and from the LHPC taken from Ref. [54] (squares). The dashed line shows the parameterization of the experimental data.

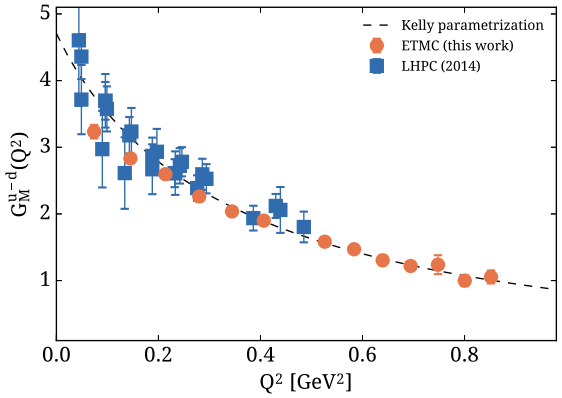

FIG. 24. Comparison of $G_M^{u-d}(Q^2)$ between results from this work (circles) and Ref. [54] (squares). The dashed line shows the parameterization of the experimental data.

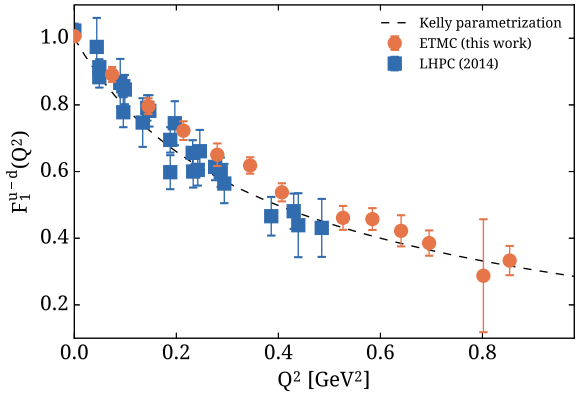

FIG. 25. Comparison of $F_1^{u-d}(Q^2)$ between results from this work (circles) and Ref. [54] (squares). The dashed line shows the parameterization of the experimental data.

method is used for their final quoted results. Within errors, we see consistent results at all Q^2 values.

In Figs. 25 and 26 we compare our results for the isovector Dirac and Pauli form factors $F_1^{u-d}(Q^2)$ and $F_2^{u-d}(Q^2)$ with those from Ref. [54]. We use Eq. (6) to obtain $F_1^{u-d}(Q^2)$ and $F_2^{u-d}(Q^2)$ from $G_E^{u-d}(Q^2)$ and $G_M^{u-d}(Q^2)$ extracted from the plateau method at the same sink-source separations used in Figs. 23 and 24. As in the case of $G_E^{u-d}(Q^2)$ and $G_M^{u-d}(Q^2)$ we see agreement between these two calculations. We also note that the discrepancy with experiment of $G_M^{u-d}(Q^2)$ at low Q^2 values carries over to $F_2^{u-d}(Q^2)$.

For the isoscalar case, we compare the connected contributions to the Sachs form factors with Ref. [54] in Figs. 27 and 28. The agreement between the two lattice formulations is remarkable given that the results have not been corrected for finite volume or cutoff effects. The gauge configurations used by LHPC were carried out using the same spatial lattice size as ours but with a coarser lattice

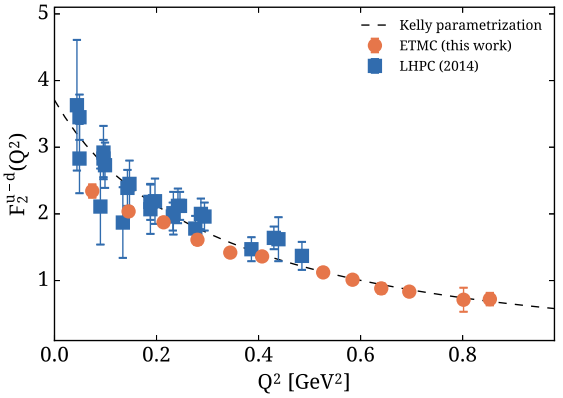

FIG. 26. Comparison of $F_2^{u-d}(Q^2)$ between results from this work (circles) and Ref. [54] (squares). The dashed line shows the parameterization of the experimental data.

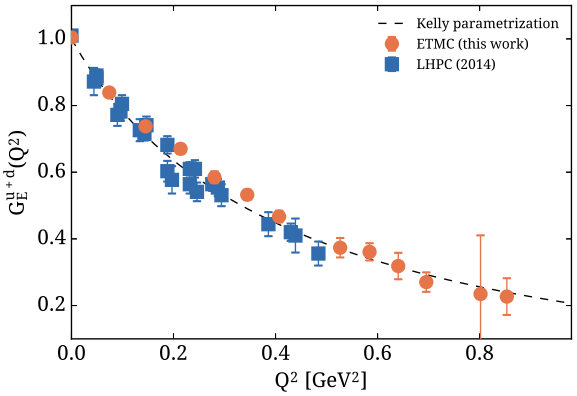

FIG. 27. Comparison of $G_E^{u+d}(Q^2)$ between results from this work (circles) and Ref. [54] (squares). The dashed line shows the parameterization of the experimental data.

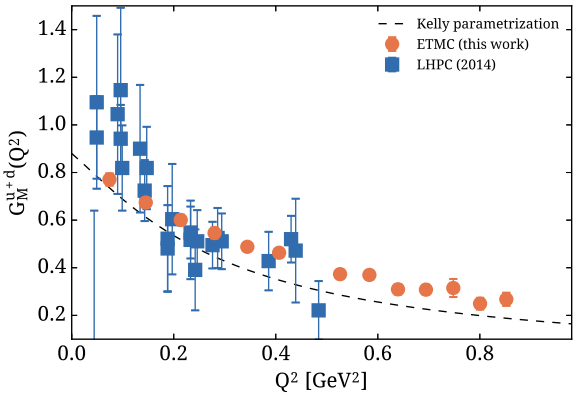

FIG. 28. Comparison of $G_M^{u+d}(Q^2)$ between results from this work (circles) and Ref. [54] (squares). The dashed line shows the parameterization of the experimental data.

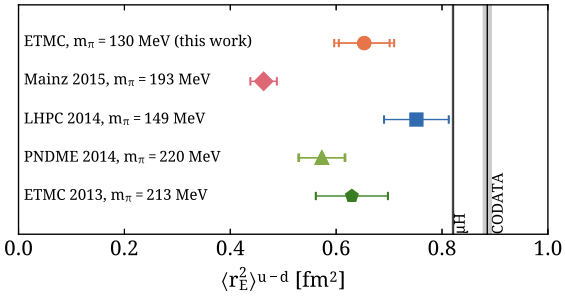

FIG. 29. Our result for $\langle r_E^2\rangle^{u-d}$ at $m_\pi = 130$ MeV (circle) compared to recent lattice results from LHPC [54] at $m_\pi = 149$ MeV (square), PNDME [52] at $m_\pi = 220$ MeV (triangle), the Mainz group [51] at $m_\pi = 193$ MeV (diamond) and ETMC [53] (pentagon). We show two error bars when systematic errors are available, with the smaller denoting the statistical error and the larger denoting the combination of statistical and systematic errors added in quadrature. The vertical band denoted with μH is the experimental result using muonic hydrogen from Ref. [2] and the band denoted with CODATA is from Ref. [57].

spacing yielding $m_\pi L = 4.2$ compared to ours of $m_\pi L = 3$. Although the LHPC results for the isovector magnetic form factor at low Q^2 are in agreement with experiment, they carry large statistical errors that do not allow us to draw any conclusion as to whether the origin of the discrepancy in our much more accurate data is due to the smaller $m_\pi L$ value.

For the radii and magnetic moment, we compare our result to recent published results, which are available for the isovector case, from Refs. [51–54]. We quote their values obtained before extrapolation to the physical point, using the smallest pion mass available. In Fig. 29, we see that the two results at physical or near-physical pion mass, namely the result of this work and from LHPC, are within one standard deviation from the spectroscopic determination of the charged radius using muonic hydrogen [2].

A similar comparison is shown in Fig. 30 for the magnetic radius. We see that all lattice results underestimate the experimental band by at most 2σ, with the exception of the LHPC value that used the summation method. Similar conclusions are drawn for the isovector

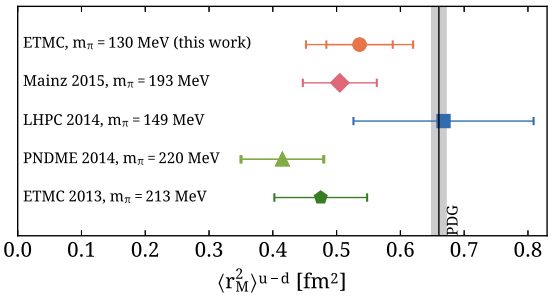

FIG. 30. Comparison of results for $\langle r_M^2\rangle^{u-d}$ with the notation of Fig. 29. The experimental band is from Ref. [57].

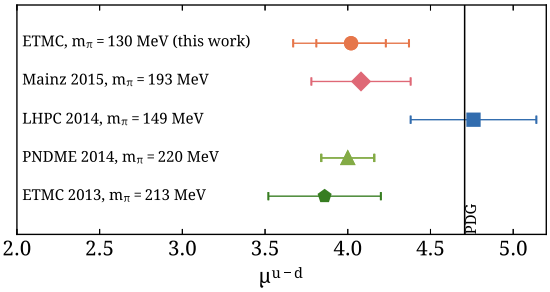

FIG. 31. Comparison of results for the isovector nucleon magnetic moment μ^{u-d} with the notation of Fig. 29.

magnetic moment $G_M(0) = \mu^{u-d} = \mu_p - \mu_n$, which we show in Fig. 31.

B. Comparison of proton form factors

Published lattice QCD results for the proton form factors at physical or near-physical pion masses are available from LHPC [54]. We compare our results in Figs. 32 and 33 for

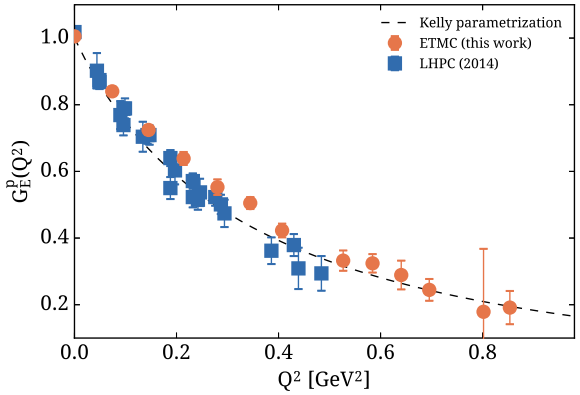

FIG. 32. Comparison of $G_E^p(Q^2)$ between results from this work (circles) and Ref. [54] (squares). The dashed line shows the parameterization of the experimental data.

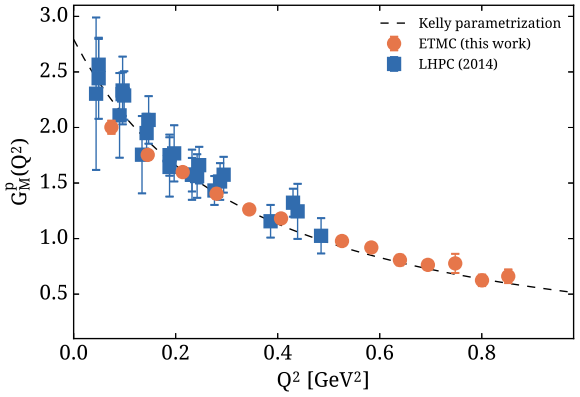

FIG. 33. Comparison of $G_M^p(Q^2)$ between results from this work (circles) and Ref. [54] (squares). The dashed line shows the parameterization of experimental data.

the proton electric and magnetic Sachs form factors, respectively. We see agreement with their results and note that their relatively larger errors at small Q^2 for the case of the magnetic form factor are consistent with both the experimentally determined curve and our results.

V. SUMMARY AND CONCLUSIONS

A first calculation of the isovector and isoscalar electromagnetic Sachs nucleon form factors including the disconnected contributions is presented directly at the physical point using an ensemble of $N_f = 2$ twisted mass fermions at maximal twist at a volume of $m_\pi L \simeq 3$. Using five sink-source separations for $G_E(Q^2)$ between 0.94 fm and 1.69 fm, we confirm our previous findings that excited state contributions require a separation larger than ∼1.5 fm to be sufficiently suppressed. For the case of $G_M(Q^2)$ we use three sink-source separations between 0.94 fm and 1.31 fm and observe that for the isovector no excited state effects are present within statistical errors, while for the connected isoscalar, the largest separation of $t_s = 1.31$ fm is sufficient for their suppression. Our results for both the isovector and isoscalar $G_E(Q^2)$ lie higher than experiment by about a standard deviation. This may be due to small residual excited state contamination since this difference is found to decrease as the sink-source separation increases. Our results for $G_M^{u-d}(Q^2)$ at the two lowest Q^2 values underestimate the experimental ones but are in agreement for $Q^2 > 0.2$ GeV^2. Volume effects are being investigated to determine whether these could be responsible for this discrepancy.

The isoscalar matrix element requires both connected and disconnected contributions, the latter requiring an order of magnitude more statistics. We have computed the disconnected contributions to $G_E^{u+d}(Q^2)$ and $G_M^{u+d}(Q^2)$ for the first four nonzero momentum transfers up to $Q^2 = 0.28$ GeV^2 and find that their magnitude is smaller or comparable to the statistical error of the connected contribution. We include the disconnected contributions to combine isovector and isoscalar matrix elements and obtain the proton and neutron electromagnetic Sachs form factors at the physical point.

We have used two methods to fit the Q^2-dependence of our data, both a dipole ansatz and the z expansion. These two methods yield consistent results, however the latter method yields parameters with larger statistical errors. Using the dipole fits to determine the electric and magnetic radii, as well as the magnetic moment, we find agreement with other recent lattice QCD results for the isovector case, and are within 2σ with the experimental determinations. Our result for the proton electric charge radius $\langle r_E^2\rangle^p = 0.589(39)(33)$ fm^2, is two sigmas smaller than the muonic hydrogen determination [58] of $\langle r_p^2\rangle = 0.7071(4)(5)$ fm^2, which may be due to remaining excited state effects or volume effects, which will be investigated further.

TABLE VII. Our final results for the isovector ($p-n$), isoscalar ($p+n$), proton (p) and neutron (n) electric radius ($\langle r_E^2\rangle$), magnetic radius ($\langle r_M^2\rangle$) and magnetic moment (μ). The first error is statistical and the second a systematic due to excited state contamination.

	$\langle r_E^2\rangle$ [fm^2]	$\langle r_M^2\rangle$ [fm^2]	μ
p-n	0.653(48)(30)	0.536(52)(66)	4.02(21)(28)
$p+n$	0.537(53)(38)	0.394(82)(42)	0.870(60)(39)
p	0.589(39)(33)	0.506(51)(42)	2.44(13)(14)
n	−0.038(34)(6)	0.586(58)(75)	−1.58(9)(12)

Our final results are collected in Table VII. We plan to analyze the electromagnetic form factors using both an ensemble of $N_f = 2$ twisted mass clover-improved fermions simulated at the same pion mass and lattice spacing as the ensemble analyzed in this work but with a lattice size of $64^3 \times 128$, yielding $m_\pi L = 4$ as well as with an $N_f = 2+1+1$ ensemble of finer lattice spacing. In addition, we are investigating improved techniques for the computation of the disconnected quark loops at the physical point. These future calculations will allow for further checks of lattice artifacts and resolve the remaining small tension between lattice QCD and experimental results for these important benchmark quantities.

ACKNOWLEDGMENTS

We would like to thank the members of the ETM Collaboration for a most enjoyable collaboration. We acknowledge funding from the European Union's Horizon 2020 research and innovation program under the Marie Sklodowska-Curie Grant Agreement No. 642069. Results were obtained using Jureca, via a John-von-Neumann-Institut für Computing (NIC) allocation ECY00, HazelHen at Höchstleistungsrechenzentrum Stuttgart (HLRS) and SuperMUC at the Leibniz-Rechenzentrum (LRZ), via Gauss allocations with ids 44066 and 10862, Piz Daint at Centro Svizzero di Calcolo Scientifico (CSCS), via projects with ids s540, s625 and s702, and resources at Centre Informatique National de l Enseignement Supérieur (CINES) and Institute for Development and Resources in Intensive Scientific Computing (IDRIS) under allocation 52271. We thank the staff of these centers for access to the computational resources and for their support.

APPENDIX: TABLES OF RESULTS

TABLE VIII. Results for the isovector $G_E(Q^2)$ using the plateau method for five sink-source separations and the summation and two-state fit methods fitted to all separations. Results where the operand of the square root in Eq. (9) becomes negative are denoted with "NA".

	Plateau, t_s [fm]					Summation	Two-state
Q^2 [GeV^2]	0.94	1.13	1.31	1.50	1.69	[0.94, 1.69]	[1.13, 1.69]
0.000	0.9982(08)	0.998(2)	0.996(41)	1.003(4)	1.006(8)	1.000(6)	-
0.074	0.8460(31)	0.832(6)	0.826(11)	0.819(15)	0.841(23)	0.798(20)	0.849(18)
0.145	0.7337(34)	0.713(6)	0.703(12)	0.701(16)	0.711(24)	0.664(21)	0.717(17)
0.214	0.6423(45)	0.618(8)	0.598(15)	0.615(21)	0.608(29)	0.556(26)	0.617(19)
0.280	0.5753(54)	0.553(10)	0.549(19)	0.514(24)	0.521(36)	0.483(35)	0.535(22)
0.345	0.5222(43)	0.503(7)	0.497(15)	0.461(19)	0.478(26)	0.435(26)	0.474(16)
0.407	0.4761(49)	0.456(8)	0.450(17)	0.391(20)	0.378(30)	0.357(30)	0.407(19)
0.527	0.4000(62)	0.380(12)	0.379(22)	0.326(31)	0.291(39)	0.283(49)	0.334(24)
0.584	0.3676(57)	0.353(10)	0.365(22)	0.265(27)	0.287(37)	0.269(42)	0.296(22)
0.640	0.3500(67)	0.338(13)	0.339(25)	0.256(35)	0.260(53)	0.229(52)	0.292(25)
0.695	0.3273(72)	0.320(13)	0.303(26)	0.236(31)	0.219(43)	0.208(54)	0.279(26)
0.749	0.284(11)	0.282(20)	0.343(47)	0.138(68)	NA	NA	0.181(46)
0.802	0.2847(85)	0.262(16)	0.215(28)	0.196(49)	0.12(21)	0.058(79)	0.203(35)
0.853	0.2707(81)	0.273(15)	0.257(34)	0.144(33)	0.156(52)	0.160(74)	0.186(35)

TABLE IX. Results for the isovector $G_M(Q^2)$ using the plateau method for three sink-source separations and the summation and two-state fit method fitted to all separations.

	Plateau, t_s [fm]			Summation	Two-state
Q^2 [GeV^2]	0.94	1.13	1.31	[0.94, 1.31]	[0.94, 1.31]
0.074	3.225(36)	3.220(54)	3.230(99)	3.18(18)	3.292(82)
0.145	2.841(28)	2.807(38)	2.832(70)	2.73(13)	2.847(54)
0.214	2.538(26)	2.505(38)	2.596(67)	2.53(13)	2.546(54)
0.280	2.288(26)	2.281(39)	2.262(75)	2.23(13)	2.294(59)
0.344	2.098(21)	2.042(31)	2.037(55)	1.85(11)	2.033(46)
0.407	1.941(19)	1.873(32)	1.899(56)	1.67(12)	1.863(45)
0.526	1.665(20)	1.611(35)	1.583(70)	1.37(15)	1.593(50)
0.583	1.565(17)	1.515(31)	1.469(64)	1.29(14)	1.483(40)
0.640	1.481(22)	1.420(39)	1.304(77)	1.14(17)	1.354(53)
0.694	1.387(20)	1.339(37)	1.219(68)	1.12(17)	1.299(52)
0.748	1.330(25)	1.275(54)	1.23(14)	0.99(29)	1.247(58)
0.800	1.218(21)	1.128(44)	0.999(83)	0.86(22)	1.063(77)
0.852	1.173(20)	1.140(46)	1.054(98)	0.98(23)	1.116(46)

TABLE X. Results for the connected contribution to the isoscalar $G_E(Q^2)$ using the plateau method for five sink-source separations and the summation and two-state fit methods fitted to all separations. Results where the operand of the square root in Eq. (9) becomes negative are denoted with "NA".

	Plateau, t_s [fm]					Summation	Two-state
Q^2 [GeV^2]	0.94	1.13	1.31	1.50	1.69	[0.94, 1.69]	[1.13, 1.69]
0.000	0.999(0)	1.000(1)	0.999(1)	1.000(2)	1.004(3)	1.000(2)	-
0.074	0.870(1)	0.863(2)	0.855(4)	0.852(5)	0.839(9)	0.834(7)	0.874(16)
0.145	0.768(2)	0.755(3)	0.746(5)	0.746(6)	0.738(10)	0.721(9)	0.756(16)
0.214	0.688(2)	0.671(4)	0.657(7)	0.665(9)	0.670(15)	0.638(11)	0.672(12)
0.280	0.624(2)	0.609(4)	0.600(9)	0.588(12)	0.585(18)	0.570(15)	0.603(12)
0.345	0.567(2)	0.552(3)	0.544(7)	0.535(10)	0.532(16)	0.508(12)	0.537(12)
0.407	0.524(2)	0.506(4)	0.499(9)	0.476(10)	0.467(17)	0.446(14)	0.487(11)
0.527	0.450(3)	0.429(6)	0.413(13)	0.430(21)	0.373(29)	0.362(24)	0.412(11)
0.584	0.421(3)	0.408(6)	0.398(14)	0.387(19)	0.361(26)	0.356(23)	0.381(10)
0.640	0.399(4)	0.385(7)	0.357(16)	0.369(26)	0.318(40)	0.308(29)	0.357(10)
0.695	0.375(4)	0.358(8)	0.322(15)	0.321(20)	0.270(29)	0.247(26)	0.338(10)
0.749	0.352(5)	0.339(12)	0.328(31)	0.336(93)	NA	NA	0.314(16)
0.802	0.331(5)	0.302(10)	0.261(20)	0.306(41)	0.235(176)	0.189(40)	0.286(12)
0.853	0.315(5)	0.304(11)	0.275(24)	0.265(31)	0.227(55)	0.239(42)	0.278(11)

TABLE XI. Results for the connected contribution to the isoscalar $G_M(Q^2)$ using the plateau method for three sink-source separations and the summation and two-state fit method fitted to all separations.

	Plateau, t_s [fm]			Summation	Two-state
Q^2 [GeV^2]	0.94	1.13	1.31	[0.94, 1.31]	[0.94, 1.31]
0.074	0.756(10)	0.760(17)	0.771(26)	0.777(54)	0.781(25)
0.145	0.669(8)	0.660(13)	0.674(21)	0.644(40)	0.671(19)
0.214	0.602(8)	0.593(13)	0.601(22)	0.584(44)	0.597(19)
0.280	0.551(8)	0.544(12)	0.546(23)	0.547(46)	0.544(19)
0.344	0.501(6)	0.484(10)	0.488(18)	0.448(36)	0.483(15)
0.407	0.465(6)	0.451(10)	0.463(18)	0.412(38)	0.455(15)
0.526	0.402(6)	0.386(11)	0.373(21)	0.339(50)	0.380(18)
0.583	0.377(5)	0.360(10)	0.370(20)	0.334(47)	0.357(14)
0.640	0.360(6)	0.339(12)	0.309(22)	0.293(52)	0.325(17)
0.694	0.334(6)	0.323(11)	0.308(21)	0.291(55)	0.324(16)
0.748	0.317(8)	0.304(16)	0.315(38)	0.332(90)	0.302(22)
0.800	0.299(6)	0.280(13)	0.249(25)	0.258(74)	0.269(22)
0.852	0.280(6)	0.275(13)	0.268(28)	0.284(73)	0.270(17)

[1] V. Punjabi, C. F. Perdrisat, M. K. Jones, E. J. Brash, and C. E. Carlson, The structure of the nucleon: Elastic electromagnetic form factors, Eur. Phys. J. **A51**, 79 (2015).

[2] R. Pohl, A. Antognini, F. Nez, F. D. Amaro, F. Biraben *et al.*, The size of the proton, Nature (London) **466**, 213 (2010).

[3] R. Pohl *et al.*, Laser spectroscopy of muonic deuterium, Science **353**, 669 (2016).

[4] A. Abdel-Rehim *et al.*, First physics results at the physical pion mass from $N_f = 2$ Wilson twisted mass fermions at maximal twist, Phys. Rev. D **95**, 094515 (2017).

[5] R. Frezzotti and G. C. Rossi, Chirally improving Wilson fermions. 1. O(a) improvement, J. High Energy Phys. 08 (2004) 007.

[6] R. Frezzotti, P. A. Grassi, S. Sint, and P. Weisz, Lattice QCD with a chirally twisted mass term, J. High Energy Phys. 08 (2001) 058.

[7] R. J. Hill and G. Paz, Model independent extraction of the proton charge radius from electron scattering, Phys. Rev. D **82**, 113005 (2010).
[8] C. Alexandrou, S. Gusken, F. Jegerlehner, K. Schilling, and R. Sommer, The static approximation of heavy-light quark systems: A systematic lattice study, Nucl. Phys. **B414**, 815 (1994).
[9] S. Gusken, U. Low, K. H. Mutter, R. Sommer, A. Patel, and K. Schilling, Nonsinglet axial vector couplings of the baryon octet in lattice QCD, Phys. Lett. B **227**, 266 (1989).
[10] A. Abdel-Rehim *et al.*, Nucleon and pion structure with lattice QCD simulations at physical value of the pion mass, Phys. Rev. D **92**, 114513 (2015).
[11] A. Abdel-Rehim, C. Alexandrou, M. Constantinou, K. Hadjiyiannakou, K. Jansen, Ch. Kallidonis, G. Koutsou, and A. Vaquero Aviles-Casco, Direct Evaluation of the Quark Content of Nucleons from Lattice QCD at the Physical Point, Phys. Rev. Lett. **116**, 252001 (2016).
[12] C. Alexandrou, G. Koutsou, J. W. Negele, and A. Tsapalis, The nucleon electromagnetic form factors from lattice QCD, Phys. Rev. D **74**, 034508 (2006).
[13] C. Alexandrou, M. Brinet, J. Carbonell, M. Constantinou, P. A. Harraud, P. Guichon, K. Jansen, T. Korzec, and M. Papinutto, Nucleon electromagnetic form factors in twisted mass lattice QCD, Phys. Rev. D **83**, 094502 (2011).
[14] C. Alexandrou and C. Kallidonis, Low-lying baryon masses using $N_f = 2$ twisted mass clover-improved fermions directly at the physical point (to be published).
[15] J. J. Kelly, Simple parametrization of nucleon form factors, Phys. Rev. C **70**, 068202 (2004).
[16] W. M. Alberico, S. M. Bilenky, C. Giunti, and K. M. Graczyk, Electromagnetic form factors of the nucleon: New fit and analysis of uncertainties, Phys. Rev. C **79**, 065204 (2009).
[17] T. Sato, D. Uno, and T. S. H. Lee, Dynamical model of weak pion production reactions, Phys. Rev. C **67**, 065201 (2003).
[18] C. Alexandrou, G. Koutsou, J. W. Negele, Y. Proestos, and A. Tsapalis, Nucleon to Delta transition form factors with $N_F = 2 + 1$ domain wall fermions, Phys. Rev. D **83**, 014501 (2011).
[19] C. Alexandrou, M. Constantinou, K. Hadjiyiannakou, K. Jansen, C. Kallidonis, G. Koutsou, K. Ottnad, and A. Vaquero, Nucleon electromagnetic and axial form factors with $N_f = 2$ twisted mass fermions at the physical point, *Proc. Sci.*, LATTICE2016 (2016) 154.
[20] A. Abdel-Rehim, C. Alexandrou, M. Constantinou, K. Hadjiyiannakou, K. Jansen, and G. Koutsou, Nucleon electromagnetic form factors from twisted mass lattice QCD, *Proc. Sci.*, LATTICE2014 (2015) 148.
[21] A. Abdel-Rehim, C. Alexandrou, M. Constantinou, V. Drach, K. Hadjiyiannakou, K. Jansen, G. Koutsou, and A. Vaquero, Disconnected quark loop contributions to nucleon observables in lattice QCD, Phys. Rev. D **89**, 034501 (2014).
[22] C. Alexandrou, K. Hadjiyiannakou, G. Koutsou, A. O'Cais, and A. Strelchenko, Evaluation of fermion loops applied to the calculation of the η' mass and the nucleon scalar and electromagnetic form factors, Comput. Phys. Commun. **183**, 1215 (2012).
[23] C. Alexandrou, M. Constantinou, K. Hadjiyiannakou, K. Jansen, C. Kallidonis, G. Koutsou, and A. Vaquero Aviles-Casco, The nucleon axial form factors using lattice QCD simulations with a physical value of the pion mass (to be published).
[24] J. Green, S. Meinel, M. Engelhardt, S. Krieg, J. Laeuchli, J. Negele, K. Orginos, A. Pochinsky, and S. Syritsyn, High-precision calculation of the strange nucleon electromagnetic form factors., Phys. Rev. D **92**, 031501 (2015).
[25] R. S. Sufian, Y.-B. Yang, J. Liang, T. Draper, and K.-F. Liu, Sea quarks contribution to the nucleon magnetic moment and charge radius at the physical point (to be published).
[26] A. Abdel-Rehim, C. Alexandrou, M. Constantinou, J. Finkenrath, K. Hadjiyiannakou, K. Jansen, C. Kallidonis, G. Koutsou, A. V. Avils-Casco, and J. Volmer, Disconnected diagrams with twisted-mass fermions, *Proc. Sci.*, LATTICE2016 (2016) 155.
[27] C. F. Perdrisat, V. Punjabi, and M. Vanderhaeghen, Nucleon electromagnetic form factors, Prog. Part. Nucl. Phys. **59**, 694 (2007).
[28] Z. Epstein, G. Paz, and J. Roy, Model independent extraction of the proton magnetic radius from electron scattering, Phys. Rev. D **90**, 074027 (2014).
[29] J. C. Bernauer *et al.*, Electric and magnetic form factors of the proton, Phys. Rev. C **90**, 015206 (2014).
[30] J. Golak, G. Ziemer, H. Kamada, H. Witala, and W. Gloeckle, Extraction of electromagnetic neutron form-factors through inclusive and exclusive polarized electron scattering on polarized He-3 target, Phys. Rev. C **63**, 034006 (2001).
[31] J. Becker *et al.*, Determination of the neutron electric form-factor from the reaction He-3(e,e' n) at medium momentum transfer, Eur. Phys. J. **A6**, 329 (1999).
[32] T. Eden *et al.*, Electric form factor of the neutron from the $^2H(\vec{e}, e'\vec{n})^1H$ reaction at $Q^2 = 0.255$ $(\mathrm{GeV/c})^2$, Phys. Rev. C **50**, R1749 (1994).
[33] M. Meyerhoff *et al.*, First measurement of the electric form-factor of the neutron in the exclusive quasielastic scattering of polarized electrons from polarized He-3, Phys. Lett. B **327**, 201 (1994).
[34] I. Passchier *et al.*, The Charge Form-Factor of the Neutron from the Reaction Polarized H-2(polarized e, e-prime n) p., Phys. Rev. Lett. **82**, 4988 (1999).
[35] G. Warren *et al.*, Measurement of the Electric Form-Factor of the Neutron at $Q^2 = 0.5$ and 1.0 GeV^2/c^2, Phys. Rev. Lett. **92**, 042301 (2004).
[36] H. Zhu *et al.*, A Measurement of the Electric Form-Factor of the Neutron through Polarized-d (polarized-e, e-prime n)p at $Q^2 = 0.5(\mathrm{GeV/c})^2$, Phys. Rev. Lett. **87**, 081801 (2001).
[37] B. Plaster *et al.*, Measurements of the neutron electric to magnetic form-factor ratio G_{E_n}/G_{M_n} via the H-2(polarized-e, e-prime,polarized-n)H-1 reaction to $Q^2 = 1.45(\mathrm{GeV/c})^2$, Phys. Rev. C **73**, 025205 (2006).
[38] R. Madey *et al.*, Measurements of G_E^n/G_M^n from the H-2 (polarized-e,e-prime polarized-n) Reaction to $Q^2 = 1.45\,(\mathrm{GeV/c})^2$, Phys. Rev. Lett. **91**, 122002 (2003).
[39] D. Rohe *et al.*, Measurement of the Neutron Electric Form-Factor G_{en} at $0.67\,(\mathrm{GeV/c})^2$ via $^3\overrightarrow{He}\,(\vec{e}, e'n)$, Phys. Rev. Lett. **83**, 4257 (1999).

[40] J. Bermuth *et al.*, The Neutron charge form-factor and target analyzing powers from polarized-He-3 (polarized-e,e-prime n) scattering, Phys. Lett. B **564**, 199 (2003).
[41] D. I. Glazier *et al.*, Measurement of the electric form-factor of the neutron at $Q^2 = 0.3(\mathrm{GeV/c})^2$ to $0.8(\mathrm{GeV/c})^2$, Eur. Phys. J. **A24**, 101 (2005).
[42] C. Herberg *et al.*, Determination of the neutron electric form-factor in the D(e,e' n)p reaction and the influence of nuclear binding, Eur. Phys. J. **A5**, 131 (1999).
[43] R. Schiavilla and I. Sick, Neutron charge form-factor at large q^2, Phys. Rev. C **64**, 041002 (2001).
[44] M. Ostrick *et al.*, Measurement of the Neutron Electric Form-Factor $G_{E,n}$ in the Quasifree $^2H(\vec{e}, e'\vec{n})p$ Reaction, Phys. Rev. Lett. **83**, 276 (1999).
[45] B. Anderson *et al.*, Extraction of the neutron magnetic form-factor from quasi-elastic $^3\overrightarrow{He}(\vec{e}, e')$ at $Q^2 = 0.1$–$0.6\ (\mathrm{GeV}/c)^2$, Phys. Rev. C **75**, 034003 (2007).
[46] H. Gao *et al.*, Measurement of the neutron magnetic form-factor from inclusive quasielastic scattering of polarized electrons from polarized ^3He, Phys. Rev. C **50**, R546 (1994).
[47] H. Anklin *et al.*, Precision measurement of the neutron magnetic form-factor, Phys. Lett. B **336**, 313 (1994).
[48] H. Anklin *et al.*, Precise measurements of the neutron magnetic form-factor, Phys. Lett. B **428**, 248 (1998).
[49] G. Kubon *et al.*, Precise neutron magnetic form-factors, Phys. Lett. B **524**, 26 (2002).
[50] R. Alarcon, Nucleon form factors and the BLAST experiment, Eur. Phys. J. A **32**, 477 (2007).
[51] S. Capitani, M. Della Morte, D. Djukanovic, G. von Hippel, J. Hua, B. Jger, B. Knippschild, H. B. Meyer, T. D. Rae, and H. Wittig, Nucleon electromagnetic form factors in two-flavor QCD, Phys. Rev. D **92**, 054511 (2015).
[52] T. Bhattacharya, S. D. Cohen, R. Gupta, A. Joseph, H.-W. Lin, and B. Yoon, Nucleon charges and electromagnetic form factors from $2 + 1 + 1$-flavor lattice QCD, Phys. Rev. D **89**, 094502 (2014).
[53] C. Alexandrou, M. Constantinou, S. Dinter, V. Drach, K. Jansen, C. Kallidonis, and G. Koutsou, Nucleon form factors and moments of generalized parton distributions using $N_f = 2 + 1 + 1$ twisted mass fermions, Phys. Rev. D **88**, 014509 (2013).
[54] J. R. Green, J. W. Negele, A. V. Pochinsky, S. N. Syritsyn, M. Engelhardt, and S. Krieg, Nucleon electromagnetic form factors from lattice QCD using a nearly physical pion mass, Phys. Rev. D **90**, 074507 (2014).
[55] Y.-C. Jang, T. Bhattacharya, R. Gupta, B. Yoon, H.-W. Lin, and Pndme Collaboration, Nucleon vector and Axial-vector form factors, *Proc. Sci.*, LATTICE2016 (2016) 178.
[56] M. Abramczyk, M. Lin, A. Lytle, and S. Ohta, Nucleon structure from $2 + 1$-flavor dynamical DWF ensembles, *Proc. Sci.*, LATTICE2016 (2016) 150.
[57] P. J. Mohr, D. B. Newell, and B. N. Taylor, CODATA recommended values of the fundamental physical constants: 2014, Rev. Mod. Phys. **88**, 035009 (2016).
[58] A. Antognini *et al.*, Proton structure from the measurement of $2S - 2P$ transition frequencies of muonic hydrogen, Science **339**, 417 (2013).